Universidade de Aveiro Departamento de Engenharia de Materiais e Cerâmica
Ano 2013

BENEDIKT REINHOLD SYKORA

INFLUÊNCIA DA ORIENTAÇÃO DO EMISSOR EM OLEDs BASEADOS EM PERILENO

INFLUENCE OF EMITTER ORIENTATION IN PERYLENE BASED OLEDs

Universidade de Aveiro Departamento de Engenharia de Materiais e Cerâmica
Ano 2013

BENEDIKT REINHOLD SYKORA

INFLUÊNCIA DA ORIENTAÇÃO DO EMISSOR EM OLEDs BASEADOS EM PERILENO

INFLUENCE OF EMITTER ORIENTATION IN PERYLENE BASED OLEDs

Dissertação apresentada à Universidade de Aveiro para cumprimento dos requisitos necessários à obtenção do grau de Mestre em Ciência e Engenharia de Materiais, realizada sob a orientação científica do Professor Doutor Wolfgang Brütting, Professor Catedrático do Institut für Physik da Universität Augsburg, e do Doutor Filipe Miguel Henriques Lebre Ramos Figueiredo, Investigador Auxiliar do Centro de Investigação em Materiais Cerâmicos e Compósitos da Universidade de Aveiro.

Financial support by the European Erasmus Mundus Master Program called FAME.

o júri

presidente

Prof.ª Dr.ª Ana Margarida Madeira Viegas de Barros Timmons
professora Auxilar do Departamento de Química da Universidade do Aveiro

Prof. Jorge Ribeiro Frade
professor Catedrático do Departamento de Engenharia de Materiais e Cerâmica da Universidade do Aveiro

Prof. Dr. Wolfgang Brütting
professor Catedrático do Institut für Physik da Universität Augsburg

Dr. Filipe Miguel Henrique Lebre Ramos Figueiredo
invesigador Auxillar do Centro de Invesitigacao em Materiais Cerâmicos e Compósitos/ Departamento de Engenharia de Materiais e Cerâmica da Universidade do Aveiro

agradecimentos

First of all I want to thank Prof. Dr. Brütting for giving me the opportunity to perform research in this interesting and recent topic about OLEDs. I also want to say thank you to Christian Mayr for the assistance during the complete research period. My thanks goes also to Prof.[a] Ana Barros and to Prof. Jorge Ribeiro for being part of the jury. A special thank you goes to Filipe Figueiredo for the assistance and organisational help during the time of my research.

Apart from that I want to say thank you to all people who work at the group of organic semiconductors at the University of Augsburg,especially to Bert Scholz and Thersa Linderl for the help with computer software and measurement setups.

A special thank you goes to the Erasmus Mundus FAME consortium for chosing me as a scholarship holder and for the financial support by the European Union. Without this support it would have been not possible for me to attend such an interessting and advanced master program.

palavras-chave

Díodos Orgânicos Emissores de Luz (OLEDs), Polaritões de Plasmões de Superfície (SPPs), Eficiência Quântica Externa (EQE), Fotoluminescência (PL), Electroluminescência (EL)

resumo

Os díodos orgânicos emissores de luz (*organic light-emitting diodes* ou OLEDs) têm como elemento funcional um filme fino de um semicondutor orgânico para a criação de excitões (pares electrão-lacuna), que emitem luz quando relaxam. O objetivo desta dissertação de mestrado é investigar o efeito da orientação dipolar de filmes baseados em perilenos de *tetraphenyldibenzoperiflanthene* (DBP) e *diindenoperylene* (DIP), e das mesmas moléculas dispersas numa ma matriz de 5,6,11,12-tetraphenylnaphthacene (rubreno). O estudo tenta identificar uma possível relação entre o comportamento destes filmes e a eficiência do respetivo OLED. Observa-se que os filmes de DBP são amorfos, apresentam uma superfície lisa e absorvem mais luz do que os filmes de DIP, que se caracterizam por uma estrutura cristalina e uma superfície irregular. Os resultados combinados de simulações e de medições de fotoluminescência com dependência angular revelam que as moléculas de DBP apresentam orientação horizontal, estando as moléculas de DIP orientadas verticalmente. Este facto pode explicar o acoplamento mais forte das moléculas de DIP aos plasmões de superfície, em comparação com o DBP.

As características gerais dos filmes de DBP ou DIP mantêm-se mesmo quando estes são depositados nos substratos de N, N '-di(1-naftil-N,N-difenil-(1,1'-bifenil)-4,4' –diamina utilizados ma preparação dos OLEDs, o que permite a comparação direta entre as duas configurações. Os resultados obtidos com os OLEDs baseados em filmes puros de DBP ou DIP apresentam valores de eficiência quântica externa (EQE) da ordem de 0,2 e 0,04 %, respetivamente. Estes valores baixos podem explicar-se pela orientação vertical dos dipolos do DIP, conduzindo a um fator de emissão de 27% (*light outcoupling*), claramente superior ao obtido com o OLED baseado no DBP (16%).

Estas diferenças acentuam-se quando na comparação destes filmes com o comportamento dos filmes rubreno equivalentes dopados com 1% de DBP e DIP. Se por um lado não se observa nenhuma orientação dipolar preferencial no caso do DIP, as moléculas de DBP na matriz de rubreno estão quase na sua totalidade orientadas horizontalmente, o que aumenta o factor de emissão. A forte orientação preferencial no caso do DBP pode igualmente justificar o aumento de EQE de 0,2 % e 0,04% nos OLEDs com os filmes puros de DBP e DIP, para 3% e 0,5% no caso dos OLEDs com os filmes dopados. O aumento da eficiência pode também dever-se ao aumento da transferência energética da matriz de rubreno para os centros emissores. O forte efeito da orientação horizontal do emissor na eficiência dos OLEDs manifesta-se igualmente no notável aumento do factor de emissão de luz observado entre os filmes de DBP (fortemente orientados) e DIP (pouco orientados), que é de cerca de 70% no caso das camadas de emissão baseadas nos filmes puros, e de 44 % no caso dos filmes dopados.

keywords

Organic Light-Emitting Diodes (OLEDs), Surface Plasmon Polaritons (SPPs), External Quantum Efficiency (EQE), Photoluminance (PL), Electroluminance (EL)

abstract

Organic light-emitting diodes (OLEDs) contain thin films of organic semiconductors to create excitons (electron-hole-pairs), which will emit light if they de-excite. The aim of this master thesis is to investigate a possible link between the dipole orientation of perylene based films of tetraphenyldibenzoperiflanthene (DBP) and diindenoperylene (DIP), and of the same molecules dispersed in a 5,6,11,12-tetraphenylnaphthacene matrix. The study also compares the behavior of these films with that of the corresponding OLEDs.

It is shown that DBP neat films are essentially amorphous, with a rather smooth surface and they absorb more light than the DIP films, which are crystalline and have a rough surface. Simulation results and angle-dependent p-polarised photoluminescence measurements reveal that the DBP molecules have a horizontal orientation, while the DIP molecules are vertically oriented. This explains the stronger coupling of DIP molecules to the surface plasmons, when compared to the DBP molecules.

The general characteristics of the DBP or DIP films do not change when these are deposited onto N,N'-di(1-naphtyl-N,N'-diphenyl-(1,1'-biphenyl)-4,4'diamine hole transport layers used as substrates in OLEDs, thus allowing a direct comparison between both configurations.

The OLEDs comprising neat films of DBP or DIP have small external quantum efficiency (EQE) values of 0.2 and 0.04%, respectively. This is probably due to the strong vertical molecular orientation of the DBP, leading to a high light-outcoupling factor of 27%, when compared to 16% of the DIP OLED.

These differences are accentuated when comparing the behavior of the neat films with equivalent rubrene films doped with 1% of DBP or DIP. While the DIP exhibits a rather isotropic orientation, the DBP molecules are fully horizontal within the doped film, thus improving the light-outcoupling. This may partly justify the increase of EQE from 0.2% and 0.04% of the neat film OLEDs to 3% and 0.5% for the doped DBP and DIP OLEDs, respectively. The improvement of the efficiency may also be due to the enhancement of the energy transfer from the rubrene matrix to the emitter dyes.

The horizontal orientation of the emitter has a huge effect on the efficiency of perylene-based OLEDs, apparent also on the remarkable increase of the light-outcoupling of strongly oriented DBP dipoles in comparison to the weakly oriented DIP, which is of the order of 70% in the case of the neat emission layers, and of 44% in the case of the doped counterparts.

Contents

List of Figures

List of symbols

A ..... Absorption
c_0 ..... Velocity of light
d ..... Thickness
d_{hkl} ..... Crystallographic plane spacing
I_0 ..... Intensity of incident light
$I_{(z)}$ ..... Light intensity along z-direction
J ..... Current density
k ..... Extinction coefficient
k_{nr} ..... Nonradiative decay rate
k_{r} ..... Radiative decay rate
k_{x} ..... In-plane wavevector
L ..... Luminance
n ..... Refractive coefficient
q_{eff} ..... Effective radiative quantum efficiency
R ..... Reflection
R^{p} ..... Fresnel coefficient for p-polarised light
R^{s} ..... Fresnel coefficient for s-polarised light
T ..... Transmission
u ..... Order of diffraction
V ..... Voltage

Greek symbols:

α ..... Absorption coefficient
γ ..... Charge carrier balance
Δ .....Phase-shift between s- and p-polarised light
η_1 ..... Dielectric constant of medium 1
η_2 ..... Dielectric constant of medium 2
η_{EQE} ..... External quantum efficiency
η_{int} ..... Internal quantum efficiency

$\eta_{S/T}$ ..... Singlet-triplet ratio

η_{out} ..... Outcoupling factor
Θ ..... Bragg's angle of diffraction
λ .....Wavelength
ρ .....Polarisation
tanψ .....Phase difference between s- and p-polarised light
ω ..... Angular frequency

List of abbreviations

AFM ..... Atomic force microscopy
α-NPD ..... *N*,*N*'-di(1-naphtyl-*N*,*N*'-diphenyl-(1,1'-biphenyl)-4,4'diamine
BPhen .....Bathophenanthroline
DBP ..... Tetraphenyldibenzoperiflanthene
DIP ..... Diindenoperylene
EL ..... Electroluminescence
EML ..... Emission layer
EQE ..... External quantum efficiency
ETL ..... Electron transport layer
HIL ..... Hole injection layer
HOMO .....Highest occupied molecular orbital
HTL ..... Hole transport layer
ITO ..... Indium tin oxide
LUMO..... Lowest unoccupied molecular orbital
OLED .....Organic light-emitting diode
OPVD.....Organic vapor phase deposition
PEDOT:PSS.....Poly(3,4-ethylenedioxythiophene):poly(styrenesulfonate)
PL.....Photoluminescence
SPP.....Surface plasmon polariton
XRD.....X-ray diffraction

1 Preamble

This thesis was performed in the framework of the european ERASMUS MUNDUS master program called FAME (Functional and Advance Materials and Engineering). The author of the thesis attended the lectures of the third semester of this program at the university of Aveiro in Portugal. The research for this thesis was done at the group called 'Organic semiconductors' at the university of Augsburg (Germany). The thesis was finally defended in Aveiro because the final master certificate will be delivered to one part from this university. The idea of the research topic were mainly delivered by Prof. Wolfgang Brütting and PhD. student Christian Mayr, but the idea to look also at doped DIP films and OLEDs were proposed by the author of this thesis.

The aim of this thesis is to gain knowledge about the link between the orientation of perylene based emitter molecules and the efficiency of corresponding OLEDs. Thin films of the analysed organic materials are produced and characterised by x-ray diffraction, light absorption, atomic force microscopy and angle-resolved photoluminescence measurements. The coupling of the emitter molecules to surface plasmon polaritons is examined. OLEDs comprising the perylene layers are produced and analysed optically and electronically. Also their external quantum efficiency is determined and discussed. The effect of the substrate temperature during the deposition of these molecules on the orientation is examined too. Apart from that the orientation of these emitter molecules in doped layers is analysed and OLEDs comprising these emission layers are presented and discussed.
The thesis is divided into four chapters. First the basic principles of organic semiconductors and OLEDs are illustrated. The materials, the OLED production process and the characterisation techniques of the thin films and OLEDs are described in chapter 3. The obtained results of the characterisation of the neat and doped thin films and the corresponding OLEDs are presented and discussed in chapter 4. The thesis closes with a conclusion and an outlook.

2 Introduction

According to the 'Energy Efficiency Status Report 2012' lighting application was responsible for 10 % of the energy consumption for every house within the European Union [2]. This led to an energy consumption of 79.8 TWh in the year 2009. Since the closure of the ban on incandescent light bulbs in September 2012, halogen lamps, fluorescent lamps and LEDs can be used as lighting applications.
Apart from the listed lighting technologies also so called organic light-emitting diodes (OLEDs) could be used for lightening applications. The first efficient OLEDs consisting of thin organic films were developed by Tang and Van Slyke in the year 1987 [3]. Nowadays OLEDs were used as the lighting technologies for smartphone displays or TV screens. A stand alone property of OLEDs is the fact that they can be used for large area lighting application.
The orientation plays a big role in the efficiency of OLEDs. Flämich *et al.* report that only by changing the emitter orientation an increase of the efficiency of phosphorescent OLEDs by a factor of 1.5 could be achieved [4]. An increase of 45 % in external quantum efficiency (EQE) and light-outcoupling in the case of dye-doped OLEDs was reported by Frischeisen *et al.* [5].

In this chapter the basics of organic semiconductors and of OLEDs shall be presented on the one hand. On the other hand one of the most important OLED characterisation property, the external quantum efficiency (EQE) and the optical loss channels in an OLED with a focus on the coupling to surface plasmon polaritons (SPP) are described. Apart from that the Förster transfer as one example of an energy transfer mechanism in dye doped OLEDs shall be described.

2.1 Organic semiconductors

All organic semiconductors, either small molecules or polymers, have a delocalized π-electron system in common. It consists of the p_z-orbital of the sp^2 hybridised molecule [6]. The ethene molecule in Fig. 2.1 is the most simple example of such a configuration. The two carbon atoms are connected via the strong σ-bond (red orbitals) and the weak π-bond (green orbitals).

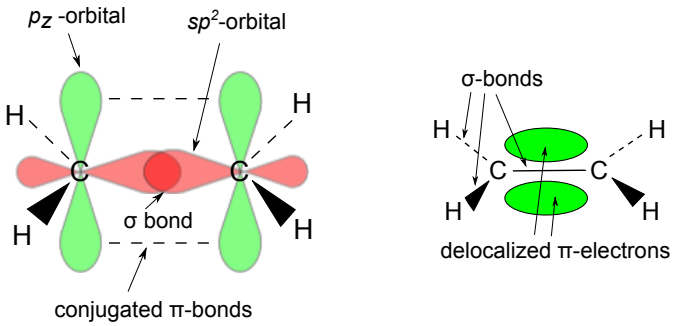

Figure 2.1: Ethene molecule and the definition of the different bonds and orbitals present in the structure.

The electrons of the π-bond can easily be excited to a higher electronic state like illustrated in Fig. 2.2. The most common excitation of an electron is from a binding π to a non-binding π^* state. Since this energy gap is of the order of a few eV the absorption or emission of radiation can take place within the visible region of the electromagnetic spectrum. The HOMO labels the highest occupied molecular orbital while LUMO is the lowest unoccupied molecular orbital.

Now some basic properties of this kind of materials shall be presented by referring to the book written by M. Schwörer and H. C. Wolf [7]. Organic semiconductors can either be polycrystalline or amorphous, but the latter case is more common. Normally they are low weight materials with a rather low melting point. Since the electrons are not conducted via electronic bands but via a hopping process the electronic mobility is small with a typical value of $1\,\mathrm{cm}^2\ \mathrm{V}^{-1}\ \mathrm{s}^{-1}$ for electrons or holes at 300 K.

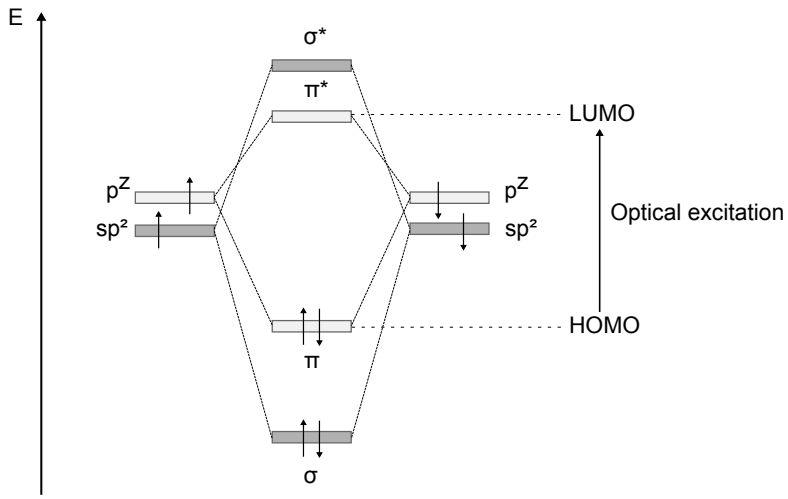

Figure 2.2: Energetic scheme of the ethene molecule with binding σ- and π-bonds and non-binding σ*- and π*-bonds.

2.2 Organic light emitting diodes

Organic light-emitting diodes are electronic devices that emit light if they are electrically driven. This method is called electroluminescence (EL).
Fig. 2.3 shows a scheme of the working principle of a simplified one layer OLED. This principle can be divided into four basic steps [8]:

(1) Injection of charge carriers (electrons and holes)

(2) Transport of charge carriers

(3) Creation of an exciton

(4) Light emission

First electrons are injected from the cathode with a high work function $\Phi_{B,e}$ and holes from the anode with a small work function $\Phi_{B,h}$ (1). Then electrons are transported along the LUMO and holes along the HOMO of the organic layer (2) until they feel the attraction between each other and excitons are created (3). These quasi-particles are bonded electron-hole pairs.
If the electrons finally recombine with the holes the energy difference is emitted as

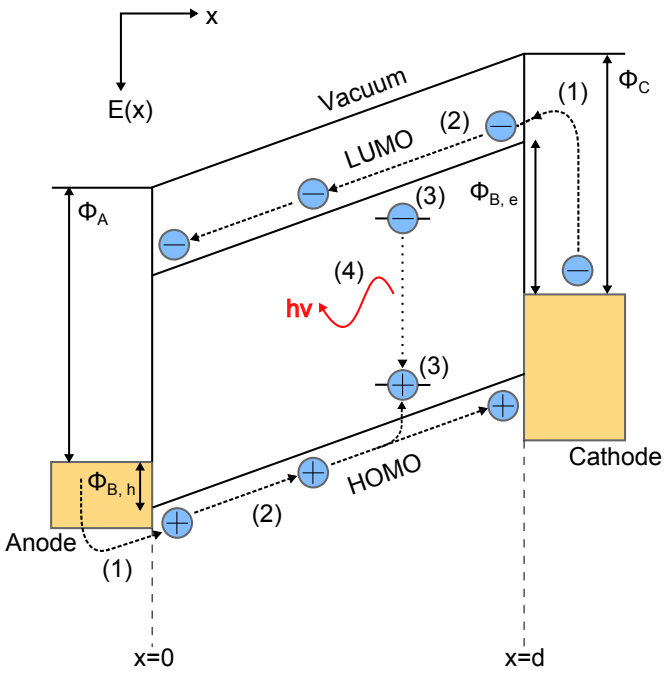

Figure 2.3: Working principle of an one layer OLED indicating the four basic steps: (1) injection of the charge carriers, (2) transport of electrons and holes, (3) creation of excitons and (4) light emission.

electromagnetic radiation (4). It should be mentioned, that the presented electronic band scheme is simplified because the conduction process is, as mentioned before, different from a simple band conduction process. In order to improve the efficiency of an OLED not only one but several organic layers with different tasks are used. One example of such a multi-layer OLED will be presented in the next chapter.

If no bias is applied on the electrodes of an OLED then there exists a built-in voltage V_{bi} that can be calculated by the difference between the two described work functions divided by the elementary charge e ($V_{\mathrm{bi}} = (\Phi_{\mathrm{B,h}} - \Phi_{\mathrm{B,e}})/e$) [8].

2.3 External quantum efficiency

The external quantum efficiency (EQE) defines the ratio between emitted photons from an OLED and the amount of charge carriers injected into the electronic device. It can be represented by equation 2.1 [9].

$$\eta_{\mathrm{EQE}} = \gamma \cdot \eta_{\mathrm{S/T}} \cdot q_{\mathrm{eff}} \cdot \eta_{\mathrm{out}} = \eta_{\mathrm{int}} \cdot \eta_{\mathrm{out}} \tag{2.1}$$

The variable γ is the charge-carrier balance, which means the balance between electrons and holes within the device. This factor can be assumed to be equal to 1 if a multi-layer stack is used. $\eta_{\mathrm{S/T}}$ labels the so called singlet-triplet ratio. This ratio has a value of 0.25 in the case of a fluorescent emitter due to spin statistics of singlet and triplet states.

The factor q_{eff} is the effective radiative quantum efficiency and can be defined according to equation 2.2 [10].

$$q_{\mathrm{eff}} = \left(\frac{k_{\mathrm{r}}}{k_{\mathrm{r}} + \sum k_{\mathrm{nr}}} \right) \tag{2.2}$$

The variables k_{nr} and k_{r} are defined as the nonradiative and radiative decay rates, respectively. This ratio therefore defines the efficiency of the luminescence.
All factors of equation 2.1, that have been presented so far can be summarised as the internal quantum efficiency η_{int}. The final factor in equation 2.1 represents the outcoupling efficiency η_{out}. Within this important factor all processes are combined which lead to the loss of produced light within an OLED. These optical loss channels are described in the next section.

2.4 Optical loss channels

Fig. 2.4 shows the different types of optical loss channels that can be present in an OLED. The values for the critical emission angle Φ that lead to total reflection between the organic/air and organic/glass interfaces can be calculated if a refractive index of air (n=1.0), glass (n=1.5) and organic (n=1.8) is assumed.

Light can only be directly emitted if the angle of emission Φ is smaller than 34°. If Φ is between 34° and 56° light is trapped within the glass substrate (substrate mode) and can be outcoupled for example by using a glass prism. In the angle section between 56° and 90° light is guided along the organic layers (waveguide mode). The last optical loss channel is the coupling to so called surface plasmons.

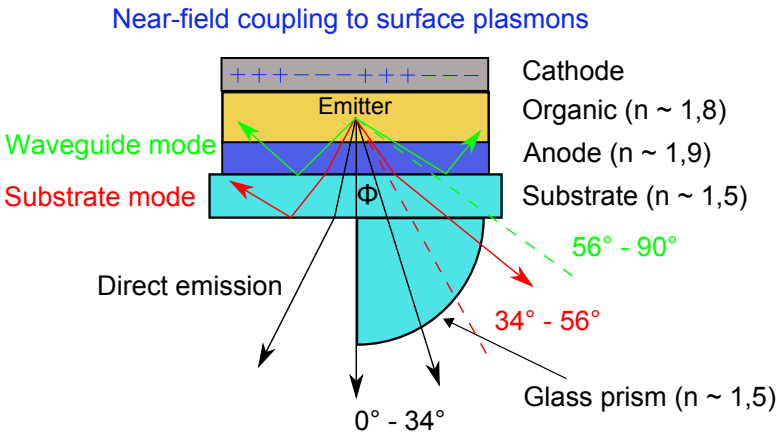

Figure 2.4: Representation of the different kinds of optical (loss) channels present in an OLED. These are the direct emission ($0°<\Phi<34°$), the substrate mode ($34°<\Phi<56°$), that can be outcoupled using a glass prism, the waveguide mode within the organic layers ($56°<\Phi<90°$) and the coupling to surface plasmons (adapted from [11]).

Surface plasmons are quasi-particles and they are more correctly called surface plasmon polaritons (SPPs) [12]. They are created if incident photons are interacting with free electrons of a metal-dielectric interface. The corresponding electromagnetic wave propagates along the interface in the µm range but decreases sharply within hundreds of nm along the z-direction. This decay of the electric field is stronger within the metal than within the dielectric material. This effect can be seen in Fig. 2.5.

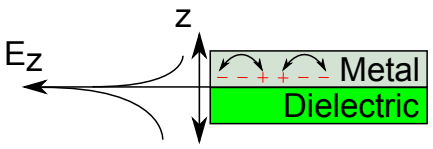

Figure 2.5: Illustration of surface plasmons at a metal-dielectric interface, that shows the decay of the electric field along the z-direction (adapted from [11]).

The dispersion relation of SPPs can be written according to equation 2.3 referring to the publication of Sambles *et al.* [13]. The variable ϵ_1 and ϵ_2 represent the dielectric contants of medium 1 and medium 2. k_x is the in-plane wavevector, ω is the angular frequency and c_0 is the velocity of light in vacuum.

$$k_x = \frac{\omega}{c_0}\left(\frac{\epsilon_1\epsilon_2}{\epsilon_1+\epsilon_2}\right)^{1/2} \tag{2.3}$$

If this surface plasmon dispersion relation is plotted for a metal/glass and a metal/air interface combined with the corresponding light lines for air and glass, Fig. 2.6 is obtained. At an angle Θ of 90° the maximum wave vector can be realised as the broken air light line with the equation $k_x = \frac{\omega}{c_0}$. It can be seen that surface plasmons can not be created by shinning light at a metal/air interface, because there is no intersection between the associated curves.

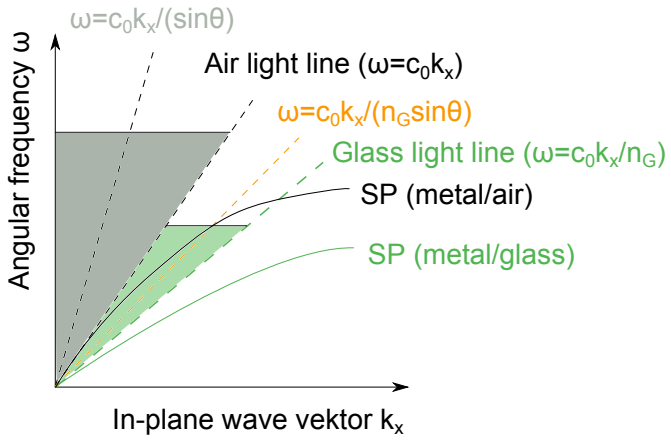

Figure 2.6: Surface plasmon dispersion relation for a metal/glass and a metal/air interface with associated light lines of air and glass (brocken lines). The glass and air light cones are illustrated as green and grey areas. If the angle of incidence increases the slope of the light line increases as well (orange and qrey line) (adapted from [11]).

This result is the reason why it is possible to create and detect surface plasmons at a glass/organic/silver/glass stack if a glass prism is attached for the outcoupling process.

2.5 Förster transfer

Since also doped emission layers were analyzed for this thesis the energy transfer between the host material as the donor and the guest material as the acceptor shall now be examined. There are two possibilities to transfer energy between the donor and the acceptor.

These are the Förster and Dexter energy transfer. Since the materials analysed in this thesis exhibit a Förster transfer mechanism, only this mechanism shall now shortly be described.

If there is an overlap between the emission spectrum of the donor and the absorption spectrum of the acceptor a so called Förster transfer can occur [14]. An excited donor molecule can first reduce its energy towards the first excited state S_1 without emission of a photon. The energy, that results from the transition from the S_1 to the ground state S_0 can be used to excite an acceptor molecule. This is a nonradiative process. The excited acceptor molecule can after the disexcitation to the S_1 state de-excite to S_1 by the emission of a photon. This mechanism is illustrated in Fig. 2.7.

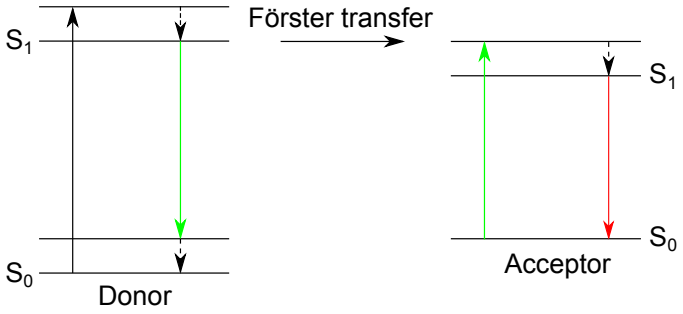

Figure 2.7: Illustration of the Förster energy transfer mechanism.

Fig. 2.8 displays the spin transitions between the donor D and the acceptor A. The stars behind the letters labels the excited state. It can be seen that no spin flip take place and it can be expressed as a singlet-singlet-transfer.

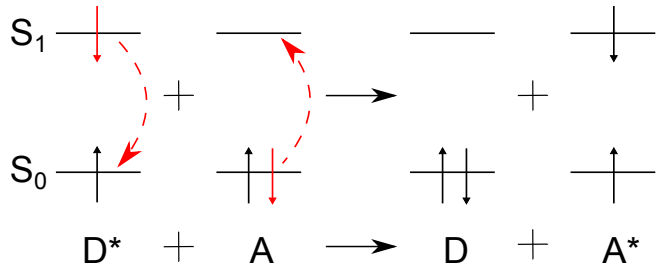

Figure 2.8: Spin transitions between the donor D and the acceptor A at a Förster transfer. It can be seen that no spin flip take place.

It should be mentioned that the Förster energy transfer can take place until a distance of around 10 nm. This distance is a lot larger than the typical distance of a Dexter transfer (<1 nm).

3 Experiment

In this chapter the used materials for the production of thin films and OLEDs are presented and the production process is described. Then the different characterisation techniques to characterise the produced films and OLEDs are discussed. The last section of this chapter presents the performed optical simulations.

3.1 Materials

As already been said in section 2.2 an efficient OLED is normally comprised of different layers with special tasks. These layers shall now be presented referring to one exemplary OLED stack, that has been analysed in this thesis (Fig. 3.1). The preparation techniques are described in the following section. This stack represents a bottom emitting diode, because the light leaves the electronic device through the glass substrate.

For this configuration of the layers it is important to know the distance between the emitter within the EML and the silver cathode that acts like a mirror. This distance can be adjusted by selecting the thickness of the ETL. The outcoupling efficiency into air depends on this distance since constructive or destructive interference between the emitted electromagnetic waves can occur. The distance from the emitter to the glass substrate, that can be selected by the thickness of the HTL, has not such a big influence on the outcoupling efficiency. The reason is that only light that travels at a higher angle than the angle of total reflection at the interface lead to reflection [11].

This fact is the reason why the thickness of α-NPD as the HTL and BPhen as the ETL has to be determined by ellipsometry measurements in order to make a comparison between

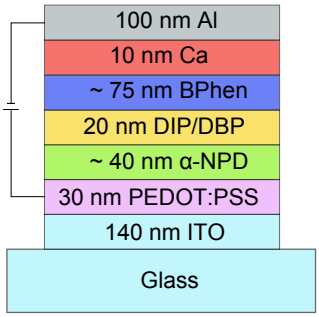

Figure 3.1: Multi-layer stack of the analysed OLEDs. Containing a glass substrate, an ITO layer as the anode, a layer of PEDOT:PSS as the hole injection layer (HIL), α-NPD as the hole transport layer (HTL), the two different emission layers (EML) DIP or DBP, BPhen as the electron transport layer (ETL) and calcium and aluminium as the cathode materials.

the DIP and DBP OLEDs possible. This difference in thickness should not exceed 10 nm to compare the different properties of the OLEDs.

As a substrate a borosilicate glass BK7 with a thickness of around 0.7 mm was used. This substrate could be directly deposited with organic layers or it was covered externally with a structured indium tin oxide (ITO) layer with a thickness of approximately 140 nm. ITO is the material of choice for the anode, because it is transparent and conducts the electrical current [15].

The polymer poly(3,4-ethylenedioxythiophene):poly (styrenesulfonate) (PEDOT:PSS) is applied on top of the structured ITO-substrate in order to improve the injection of holes, for smoothening the ITO-layer and to block the diffusion of indium ions into the successive organic layers.
In this aqueous solution PEDOT is positively charged and PSS represents the negatively charged counter-ion [16]. The chemical formula of PEDOT:PSS is displayed in Fig. 3.2.

On top of the PEDOT:PSS a layer of *N*,*N*'-di(1-naphtyl)-*N*,*N*'-diphenyl-(1,1'-biphenyl)-4,4'diamine (α-NPD) was applied by thermal evaporation. This process of evaporation of organic materials and metals will be described in section 3.3. α-NPD is a material that

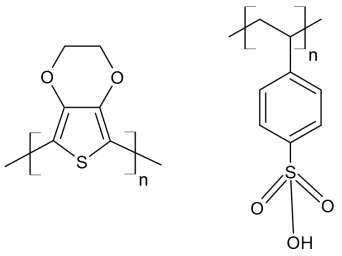

Figure 3.2: Chemical structure of poly(3,4-ethylenedioxythiophene):poly (styrenesulfonate) (PEDOT:PSS).

can be used as an efficient HTL in an OLED. Fig. 3.3 shows the chemical formula of this material.

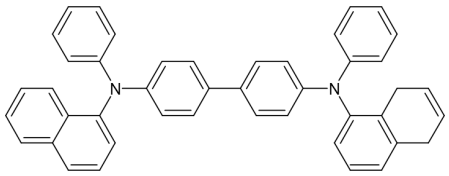

Figure 3.3: Chemical structure of *N*,*N*'-di(1-naphtyl)-*N*,*N*'-diphenyl-(1,1'-biphenyl)-4,4'diamine (α-NPD).

The two materials tetraphenyldibenzoperiflanthene (DBP) and diindenoperylene (DIP) were used as EML in the OLED stack. The structural difference between the two molecules are the 4 additional benzene rings on the side of the molecule backbone of DIP in the case of DBP. But as these benzene rings are orientated out of plane it leads to completely different physical and chemical properties. Both perylene based materials are normally used as donor materials in organic photovoltaic cells [17], [18]. The chemical structure of DBP and DIP can be seen in Fig. 3.4.

DBP and DIP was also used as a guest material, that was doped into 5,6,11,12-tetraphenyl-naphthacene. This amorphous material is also called rubrene and is used as the host material in the research of this thesis. Käfer and Witte report that it can also be used as the guest molecule and it exhibits good charge carrier properties in the form of single crystals [19]. This is the reason why it is also used as the active material in organic field-effect transistors [20]. The chemical structure of the molecule is illustrated in Fig. 3.5.

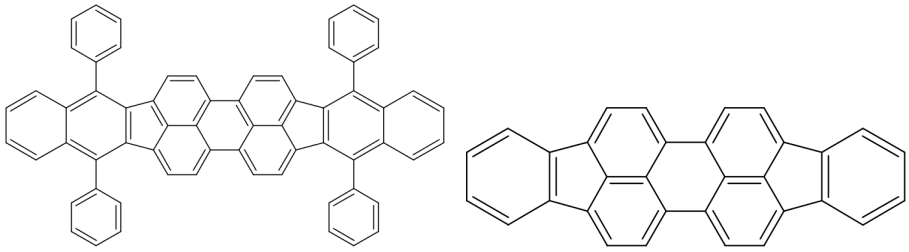

(a) DBP (b) DIP

Figure 3.4: Chemical structure of tetraphenyldibenzoperiflanthene (DBP) and diindenoperylene (DIP).

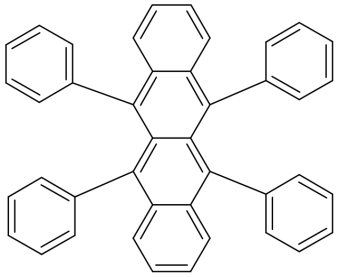

Figure 3.5: Chemical structure of 5,6,11,12-tetraphenylnaphthacene (rubrene).

The material 4,7-diphenyl-1,10-phenanthroline or also called bathophenanthroline (BPhen) is used as the ETL because of its good electron transport properties [21]. Fig. 3.6 represents the chemical formula of BPhen.

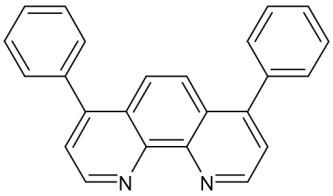

Figure 3.6: Chemical structure of bathophenanthroline (BPhen).

Calcium (Ca) is employed for the efficient injection of electrons into the device because it has a low work function [22]. In order to protect the Ca from degradation in ambient atmosphere, aluminium (Al) with a relatively low work function is deposited on top [23]. This layer is also important to ensure an electronic contact to the device and to avoid top emission of radiation.

The next two figures 3.7 and **??** show the energetic values of the layers for a complete OLED stack in the case of DBP and DIP as an EML. The single values for the work function of ITO [24], PEDOT:PSS [16] and the metals Ca [24] and Al [23] are indicated in eV. The energy level of the HOMO and LUMO of the organic layers α-NPD [25], DIP [26], DBP [27] and BPhen [28] are also introduced.

The HOMO and LUMO level of the perylene based dopants DBP in red color and DIP in green color are included into the area of rubrene as the host material. The values of the HOMO and LUMO level from rubrene are taken from the publication by Okumoto *et al.* [27].

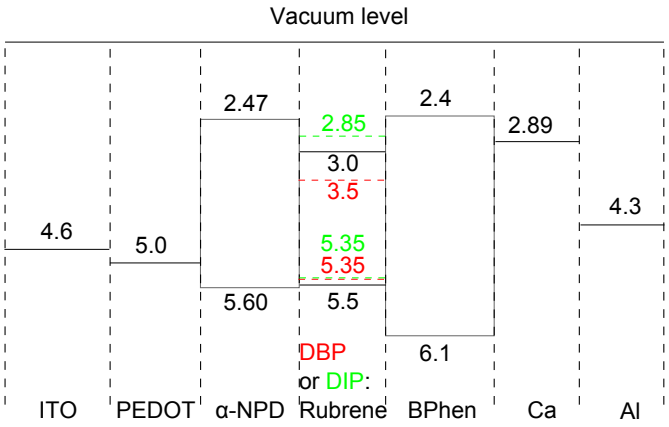

Figure 3.7: Schematic energy level diagram of an OLED with DBP (red broken lines) or DIP (green broken lines) doped into rubrene. All the values of the work functions and HOMO and LUMO levels are expressed in eV.

The materials are selected to ensure a good injection of electrons and holes into the device and to improve the creation of excitons within the EML. In the case of the doped OLEDs an energy transfer from the matrix (rubrene) to the dopant molecules (DBP and DIP) should be achieved.

3.2 OLED preparation

In this section the various steps to produce an OLED are presented. First the ITO structured glass substrates are cut with the use of a diamond cutter to 2x2 cm^2 samples. These samples are put in a glass beaker and are cleaned for 10 minutes with technical

acetone, technical isopropanol and very pure isopropanol within an ultrasonic bath. Then the samples are dried with the help of nitrogen gas and are treated for 15 min with an ozone plasma in order to remove remaining organic molecules from the solvents and to ensure a hydrophilic surface.
Another benefit from this treatment is the enhancement of the hole injection properties of ITO [15]. The samples are then coated with an aqueous solution of PEDOT:PSS using a spin-coater (5000 rpm, 60 s). The four steps of this technique are illustrated in Fig. 3.8.

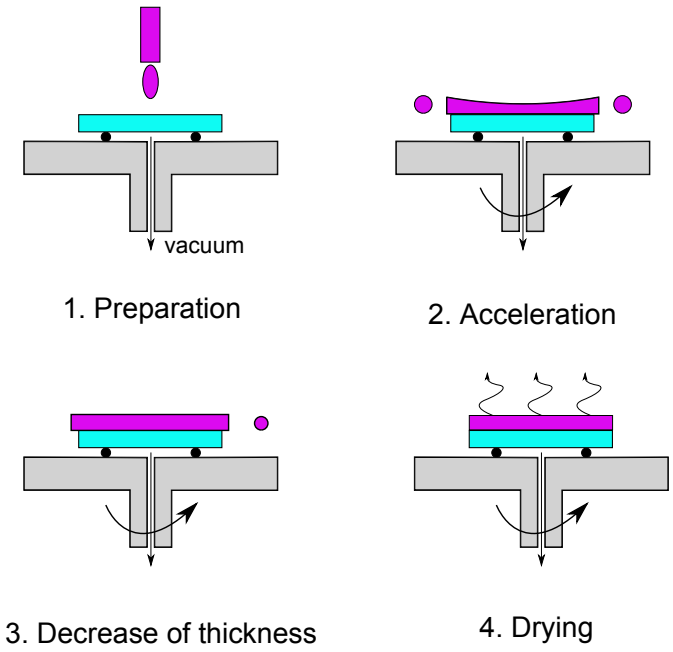

Figure 3.8: Illustration of the four steps of a spin coater: 1) preparation, 2) acceleration, 3) decrease of layer thickness and 4) drying.

Then the films are dried for 45 min at 125°C in order to evaporate the water and to achieve a thickness of PEDOT:PSS of approximately 30 nm. Apart from the cutting process all presented steps until this point take place in a clean room.

The next steps are the application of the organic materials α-NPD, DIP or DBP, BPhen and the evaporation of the metals Ca and Al within a nitrogen atmosphere and a pressure of around $2\text{x}10^{-7}$ mbar. The evaporation of the organic materials is called organic vapor phase deposition (OVPD) and shall be described with the help of Fig. 3.9.

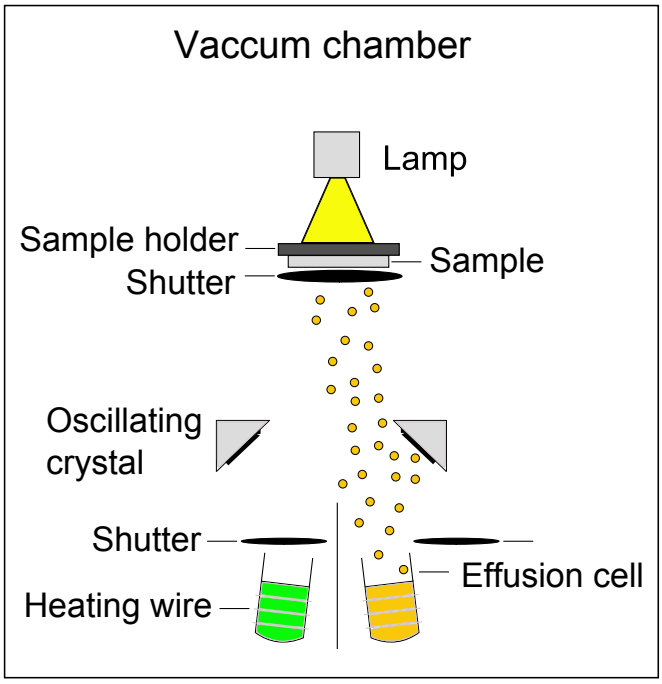

Figure 3.9: Scheme of the organic vapor phase deposition (OVPD).

The organic material in the effusion cell is heated with the help of a heating wire until it starts to evaporate. The oscillating quartz crystal measures the rate of deposition in Å/s and the amount of deposited material in nm if the shutter above the effusion cell is opened. When the deposition rate has reached the desired value, the shutter below the sample + sample holder can be opened and the deposition of the material onto the substrate starts. If the desired thickness is achieved the shutter has to be closed again. With the lamp above the sample holder the substrate of the samples can be heated during the deposition. Typical deposition rates for DIP and DBP are 0.5 Å/s and 1.0 Å/s for α-NPD, BPhen, Ca and Al.

The layers where DBP or DIP was doped into rubrene were created by co-evaporation of both materials. The deposition rate of both materials was monitored and set during the deposition to ensure a fix doping concentration. If for instance a doping concentration of 1 % was intended the deposition rate of DBP or DIP was set to be 0.02 and the deposition rate of rubrene to be 2 Å/s.

In order to determine the thickness of the produced layers of α-NPD and BPhen Si substrates were placed next to the OLED substrates. The thickness of the layers were

then determined using the method of ellipsometry.

Fig. 3.10 shows the main steps of the preparation of an OLED and the final device design. One of the four pixels with the dimension 2x2 mm^2 is illustrated red.

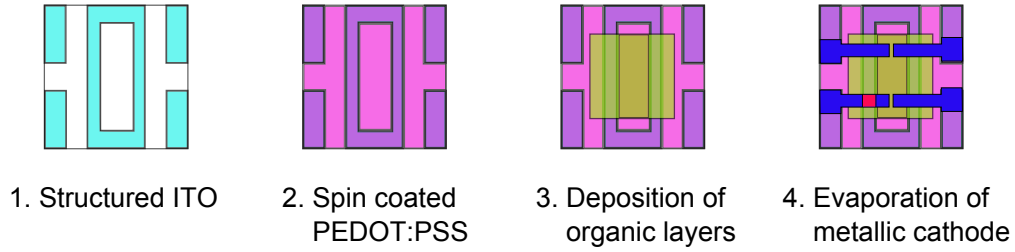

Figure 3.10: Illustration of the OLED device layout with the definition of the four pixels per device.

The final step of the OLED preparation process is the encapsulation. It is necessary to avoid the contact of the pixels with moisture and oxygen if the samples are analysed outside the nitrogen atmosphere of the glovebox. A two-component polyurethane adhesive was used to put a 1.2x1.2 cm^2 glass plate on top of the four pixels.

3.3 Thin film characterisation techniques

In this section the different techniques for the characterisation of the thin films shall be presented. These are the measurement of the absorption coefficient, x-ray diffraction (XRD), atomic force microscopy (AFM) and angle-resolved photoluminescence (PL).

In order to determine the absorption coefficient α of the DIP and DBP layers between 400 and 800 nm the transmission T and reflection R is measured by a reflectometer. The absorption coefficient for every wavelength can be calculated by Eq. 3.1 if R, T,the layer thickness of the thin organic film on a glass substrate and the absorption A (A = 1-(R+T)) of the substrate itself is known.

$$\alpha = \frac{-\ln\left(\frac{T(1-R)}{1-A}\right)}{d} \tag{3.1}$$

This equation was derived from the law of Beer and Lambert (Eq. 3.2). It describes the exponential decay of the intensity of the incident light I_0 if it is traveling a distance z within a medium with the thickness d and the absorption coefficient α.

$$I_{(z)} = I_0 \cdot \exp\left(-\alpha(\lambda)\, d\right) \tag{3.2}$$

Now the basic principle of XRD shall be presented. If an X-ray beam interacts with the regular atomic structure of a solid matter diffraction may occur. The atomic spacing has to be in the same order of magnitude than the wavelength of the incident radiation. Constructive interference occur only if the Bragg's law of diffraction is satisfied (Eq. 3.3). The parameter u labels the order of diffraction, d_{hkl} is the spacing between the crystallographic planes and Θ is the Bragg's angle of diffraction. A possible way to get access to this law is illustrated in Fig. 3.11 which shows the interaction of incident electromagnetic waves with the crystallographic planes of a solid matter.

$$u\,\lambda = 2\,d_{hkl}\sin(\Theta) \tag{3.3}$$

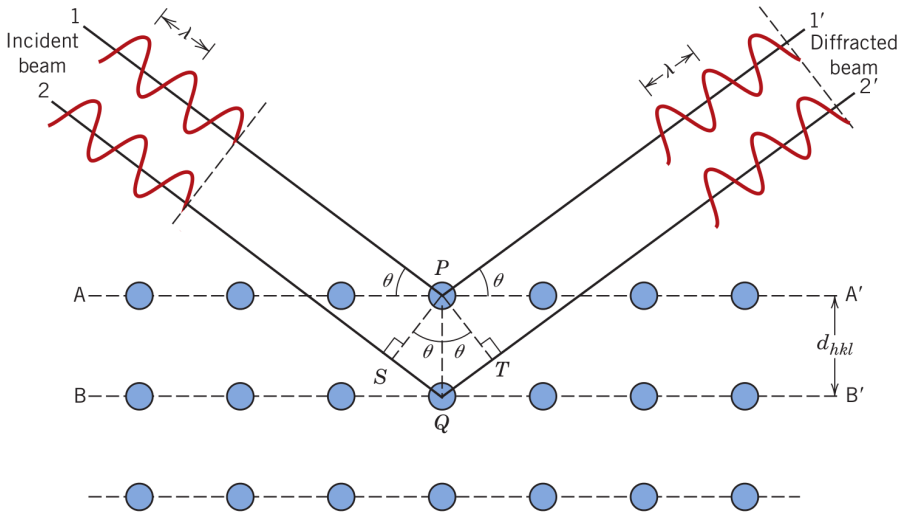

Figure 3.11: Illustration of the interaction of incident electromagnetic waves with the crystallographic planes of a solid. It is a visual representation of Bragg's law of diffraction [29].

Fig. 3.12 displays the working principle of a diffractometer in Θ/2Θ configuration. The X-ray beam is created within the X-ray source (T) is interacting with the sample (S) under the incident angle Θ and the diffracted signal is detected by a detector (C) under an angle of 2Θ. The sample and the detector are rotated during the experiment around the axis of rotation (O). Every time the angle of diffraction fulfils the Bragg's law of diffraction a diffracted signal can be measured by the detector. For the analysis of this thesis a Θ-2Θ scan was performed with a Cu cathode (40 kV, 40 mA) from 3 till 30 °.

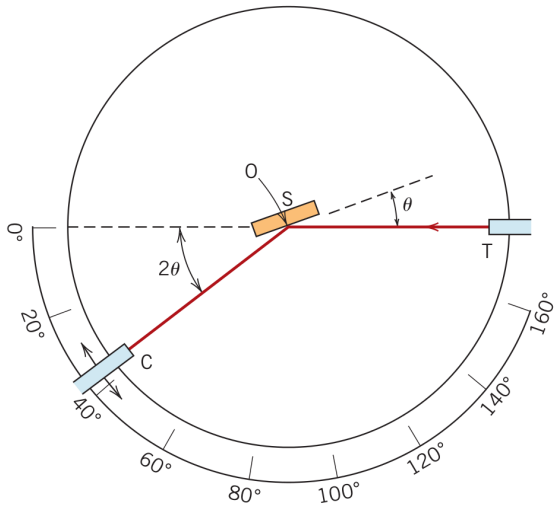

Figure 3.12: Working principle of a diffractometer, with the x-ray source (T), the sample (S) and the detector (C). The point O represents the axis of rotation of the sample and the detector [29].

The working principle of an AFM is illustrated in Fig. 3.13. The tip, that is probing the surface of the sample, is attached to a cantilever. Due to the force between sample surface and tip the cantilever is deflected. Images can be obtained if the deflection of the tip is detected with the help of a LASER and a photo diode while scanning the surface of the sample in x- or y-direction.

There are basically four different operation modes. The contact and non-contact mode and the static and dynamic mode. Since the AFM used for the research of this thesis works in non-contact and dynamic mode only these two modes will be described briefly referring to the publication of Meyer [30].
If an AFM is working in non-contact mode the distance between the surface of the sample

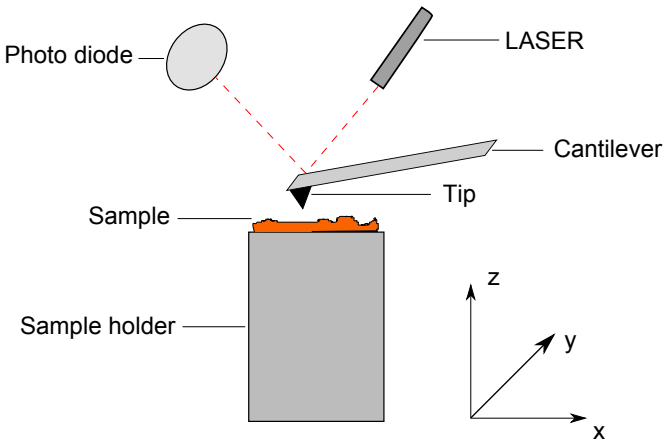

Figure 3.13: Working principle of an AFM.

and the tip is in the order of tens of nm and information about the topography of the sample can be received. Dynamic mode means, that the cantilever is vibrating near to its frequency of resonance. It should be mentioned, that attracting forces destabilise and decrease the resonance frequency while repulsive forces stabilise the motion of the cantilever and increase the resonance frequency. During the scan the frequency is kept constant and the variation in constant gradients are detected.

With the method of angle-resolved PL and corresponding simulations it is possible to get information about the orientation of emitter molecules in thin organic films. This method was developed by Frischeisen *et al.* [31].
If the transition dipole moments of molecules in an organic layer exhibit isotropic orientation they can be summarised by 1/3 p_x-, 1/3 p_y and 1/3 p_z-dipoles. The p_x and p_y-dipoles lie within the plane of the organic layer while the p_z-dipole are oriented perpendicular to the layer plane. If the molecules have an an-isotropic orientation the distribution of the transition dipole moments is different. In the case of horizontally orientated dipoles p_z-dipoles do not occur and only p_x- and p_y-dipoles in a 1:1 ratio are present. It is noteworthy that the p_x- and p_z-dipoles emit p-polarised and the p_y-dipoles emit s-polarized light. The measurement of p-polarised light gives information about the amount of vertical dipoles. It is important to mention, that all p_z-dipoles emit preferential at large angles. This is due to the fact that the radiation of dipoles is strongest in the direction perpendicular to the oscillation direction. Consequently, these p_z-dipoles couple preferentially to waveguide modes or to SPP at the interface between organic and metallic layer in an OLED structure.

This fact explains why the outcoupling efficiency can be improved if only horizontally orientated p_x- and p_y-dipoles are present in the organic emitter layer. Fig. 3.14 illustrates the different dipole moments of a molecule, that is drawn in the middle of an organic layer on a glass substrate. The excited dipole emits light, that could be p-polarised or s-polarised. The first is located inside the x-z-plane while the second kind of polarisation is located outside of this plane.

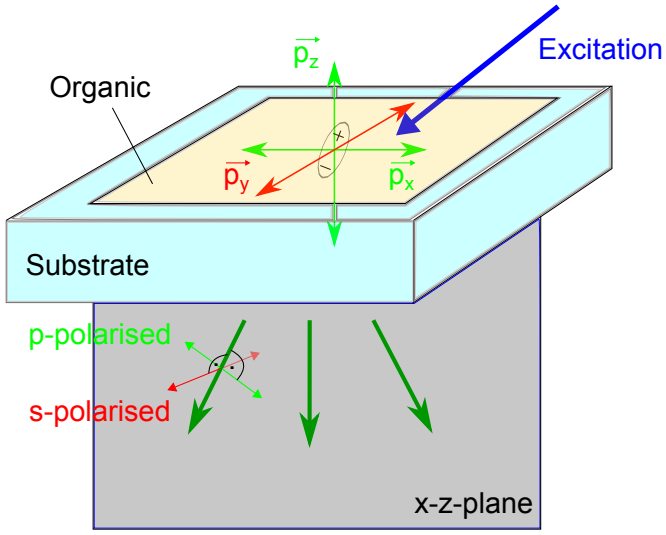

Figure 3.14: Illustration of the different dipole moments of a molecule within an organic layer and the type of polarisation of the emitted radiation [1].

Fig. 3.15 displays the experimental setup to measure the angle-resolved PL and the SPP spectra. They can be measured using a collimator, which is connected by a glass fiber cable to an optical spectrometer. The encapsulated sample is fixed on a half-sphere quartz prism with a refractive index n of 1.46. It is attached with the help of an index-matching gel (n=1.5) and installed on a rotating table, that can be rotated with a small engine and controlled by a LabView program. The use of the prism is important to uncouple the substrate modes like illustrated in Fig. 2.4. In order to excite the dipoles a 7 mW LASER diode that emits light at 375 nm was used. An additional bandpass filter was installed to avoid the emission of other wavelength ranges. The LASER was mounted on the rotating table at an angle of 45° to the substrate normal. This orientation was chosen to excite p_x and p_z-dipoles. In order to avoid the detection of the direct LASER intensity a long-pass filter with 400 nm was put between the collimator and the prism. Apart from that a polarizer was used to select between the detection of s- or p-polarised light. With

the already mentioned LabView program the settings like integration time, number of averages and the angular steps can be defined.

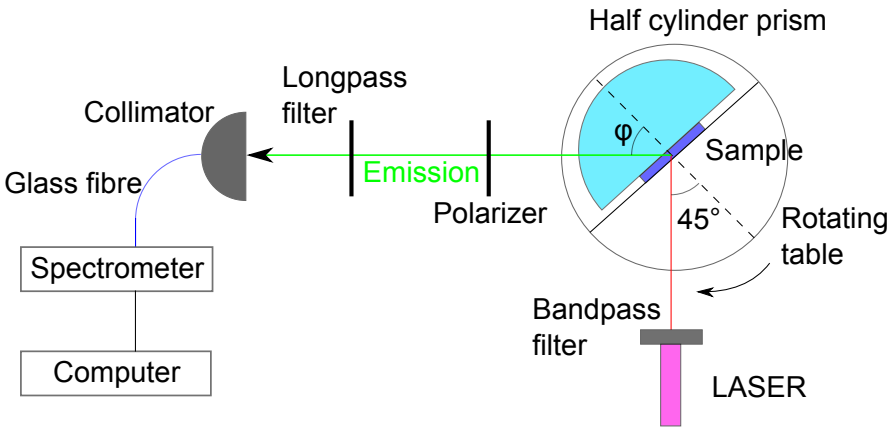

Figure 3.15: Schematic representation of the experimental setup for measuring the angle-resolved PL.

The following Fig. 3.16 shows the sample geometry to determine the angle-resolved PL spectra and the SPP spectra. The cover glass, that is glued onto the organic layer by an UV adhesive, is used to protect the organic layer against the direct radiation of the LASER. The SPPs are created at the interface between the organic and the silver layer and they can be outcoupled by the half sphere quartz glass prism.

Apart from the presented methods so far two methods were used to determine the thickness of the produced films. These are on the one hand the profilometer called 'Dektak 8' and on the other hand an ellipsometer. Both methods shall now briefly be described.

The profilometer is working according to the principle of electromechanics [32]. Fig. 3.17 illustrates the principle behind this device. The needle is moving with a constant force and velocity along the layer. On top of the needle is a tip made out of diamond with a radius of around 10 µm. The force can be varied between 0.01 and 0.15 mN. With the help of the so called LVDT-sensor (linear variable differential transformator) the vertical deflection of the needle can be measured. Consequently, an altitude profile can be obtained. The sensor is composed of one primary coil, two secondary coils and a core made out of soft iron. The core is connected to the needle. Its position compared to the combination of coils defines the magnetic flux, that is acting between the primary and the secondary coil. If a constant

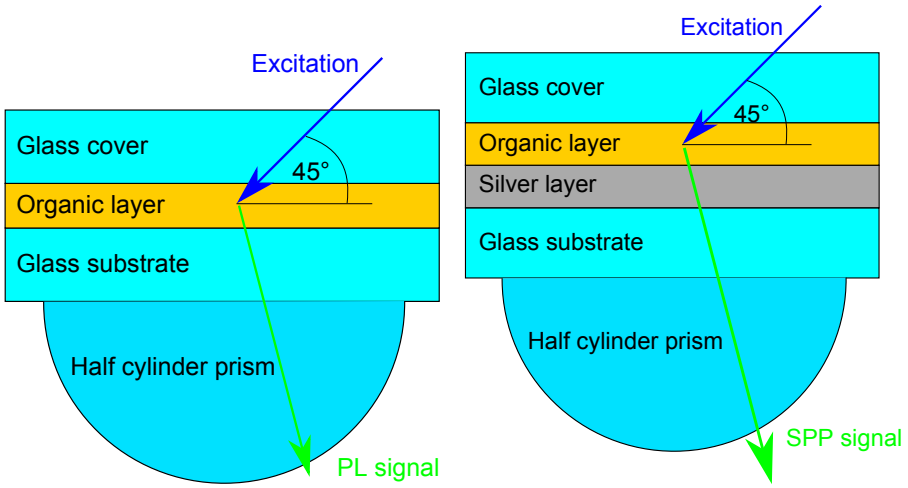

(a) PL (b) SPP

Figure 3.16: Sample geometry for the determination of the angle-resolved PL spectra (a) and for the spectra of the outcoupled SPP signal (b). The cover glass is used to protect the organic layer against the direct radiation of the LASER.

AC bias signal is applied at the primary coil an AC bias signal is induced at the secondary coil. Due to the fact that these signals can be measured precisely the deflection of the needle can be determined. An average of the layer thickness can be determined if multiple scans along the edge between the glass substrate and the organic layers are performed. In order to get a clearer edge a layer of silver was deposited onto the structured organic layer.

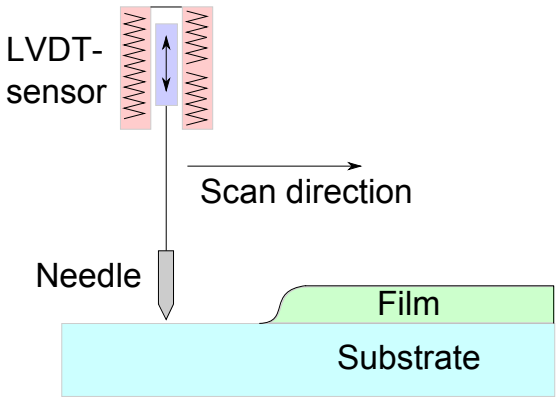

Figure 3.17: Working principle of a Dektak 8 device.

Now the basic principle of an ellipsometer shall shortly be presented. The basic setup of this device can be seen in Fig. 3.18. First circular polarised light is shining onto the sample. This light is composed of *s*- and *p*-polarised light in the same ratio but phase-shifted by an angle of 90°. The reflected light from the sample surface gets elliptically polarised. This change of the polarisation ρ can be expressed by the ratio between the two Fresnel coefficient R^{p} and R^{s} according to formula 3.4.

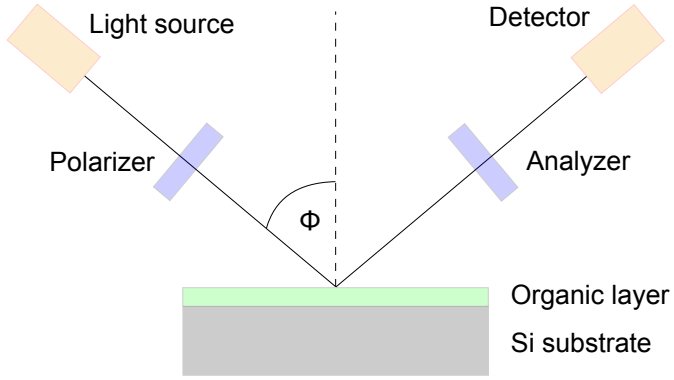

Figure 3.18: Working principle of an ellipsometer [33].

$$\rho = \frac{R^{\mathrm{p}}}{R^{\mathrm{s}}} = \tan\psi \exp(i\,\Delta) \tag{3.4}$$

The coefficient $\tan\psi$ is the absolute value of ρ and Δ expresses the difference in phase between the *s*- and *p*-polarised light.
In order to determine the thickness of the analysed layers a model with the used layers and corresponding models of oscillation has to be selected. The two variables ψ and Δ are measured in a wavelength range from 280 till 820 nm and the final thickness can be obtained after a successful fit of the measured variables. It has to be mentioned, that the layer thickness can only be determined if the organic layers are deposited onto a Si substrate, because a distinct reflection of the incident signal has to be ensured.

3.4 OLED characterisation techniques

In this section the four OLED characterisation techniques, the measurement of the current density-voltage-luminance curves, the determination of the EQE and the measurement of

the voltage and angle-resolved EL spectra shall be presented.

Fig. 3.19 displays an example of a current density-voltage-luminance curve sometimes also referred as J-V-L-curve. It was measured in a cubic box within the glovebox environment and shows a logarithmic plot of the current density J and a logarithmic plot of the luminance L as a function of the applied bias. The bias is switched from -3 to 6 V and back again with a step size of 0.1 V.

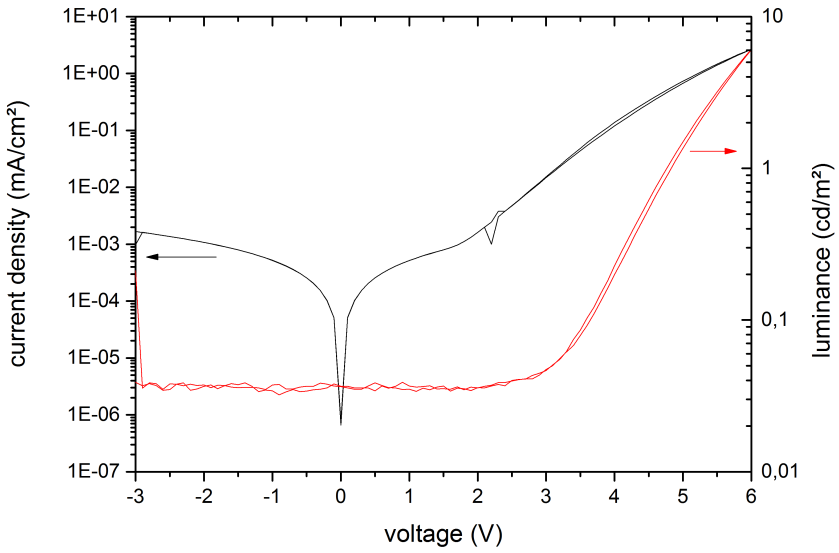

Figure 3.19: Example of a current-voltage-luminance (J-V-L) curve showing a double-logarithmic plot of the current density and the luminance as a function of the applied bias voltage.

From the figure it can be extracted that the analysed OLED exhibit a leakage current density of around 1.1E-3 mA/cm^2 at an applied bias of -3 V. If the voltage exceeds a value of 2 V, the built-in voltage, the two charge carriers are injected into the EML and the device starts to illuminate when the charge carriers recombine. The luminance in cd/m^2 could be measured using the integrated photometric filter within the cover of the box. The highest value for this OLED was measured to be 6 cd/m^2.

In order to determine the EQE of the different OLEDs first their emission spectrum has to be obtained. It was measured within an integrating or Ulbricht sphere. This sphere is used to ensure, that the light emitted by the OLED is distributed equally inside the sphere. The interior of the sphere is coated with bariumsulfate ($BaSO_4$) to guarantee a diffuse reflection. This sphere was connected by a glass fibre cable to a spectrometer. The spectrometer consists of a CCD camera, that is cooled with liquid nitrogen to ensure a good signal-to-noise ratio, three different gratings for different wavelength sensibilities and a analysing software. The spectra of the OLEDs were taken if they are operated by a voltage of 6 V.

With the help of the obtained emission spectra the EQE can be measured within the Ulbricht sphere as well. A scheme of the Ulbricht sphere and the connected devices can be seen in Fig. 3.20.

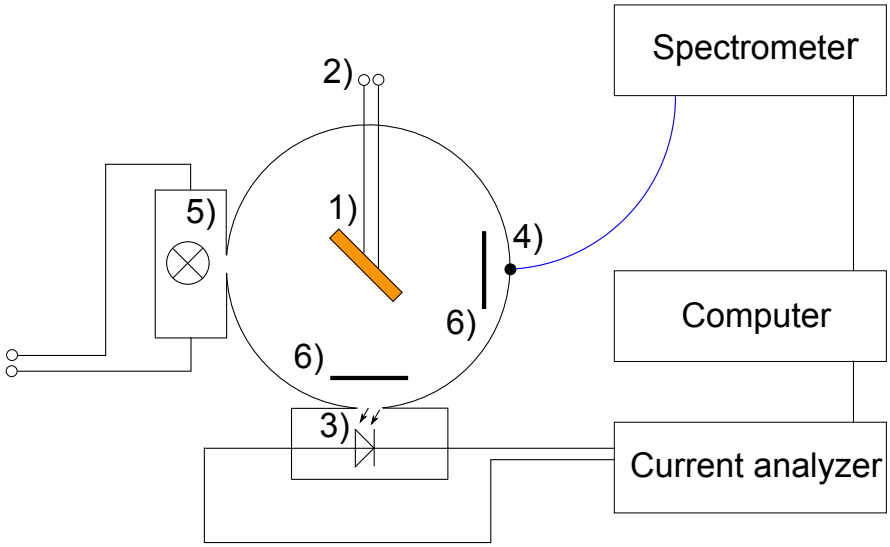

Figure 3.20: Scheme of the Ulbricht sphere and the connected devices: 1) sample holder with sample, 2) power supply, 3) photo-diode, 4) spectrometer connection, 5) calibration lamp and 6) baffles.

The edges of the OLEDs have to be coated with whiteout in order to avoid the outcoupling of substrate modes before the sample is put into the sample holder 1). The sample is connected to a power supply station 2), that power the OLED with a certain amount of current and measures the resulting voltage. The photocurrent is measured by the

connected photo-diode 3). The calibration lamp 5) was used to calibrate the spectrometer. The two baffles are installed inside the sphere to avoid the direct illumination of the photo-diode and the spectrometer connection 4).

Apart from the efficiency characterization of the produced OLEDs they were also characterised optically.
On the one hand an angle-resolved EL emission spectra from -90° to 90° were obtained using the same setup then the one for the angle-resolved PL measurements (see Fig. 3.15). The LASER, the long-pass filter and the polarizer was not used for the un-polarised measurents. The obtained emission spectra was compared to the emission spectra of an Lambertian radiator.
On the other hand the voltage dependent emission spectra of the powered OLEDs were measured inside a cubic box using a collimator and a spectrometer.

3.5 Optical simulations

Apart from the characterisation of the thin organic films and the corresponding OLEDs also optical simulations are performed. The aim of the simulations is to compare the measured data with the simulated results and to give a statement on the orientation of the emitter molecules by the analysis of a p-polarised measurement.

The software used for this purpose was developed within the group and is based on the dipole model first introduced by Sommerfeld [34]. He investigated the radiation of an electromagnetic waves sent by an antenna over the earth surface, that is assumed to be conductive.

It is assumed for the optical simulations, that the emitter molecules within the EML are excited and emit light. The directional characteristic of the molecules can be obtained. There are two extreme cases if the transition dipole moment is oriented within the x-y plane or perpendicular to it. While the first case corresponds to a perfect horizontal

orientation of the molecules, the latter case represents the directional characteristic of an upright standing molecule. The intensity of radiation is strongest perpendicular to the dipole orientation $\overrightarrow{p}$.

For further information about the theory behind this siumlation tool it shall be referred to the PhD thesis of Jörg Frischeisen [11]. To perform simulations with the software the optical constants of the analysed materials and the un-polarised 0 ° PL emission spectra of the EL are necessary. With the help of the software it is possible to build up the analysed stack (thin film or OLED), to define the EML and the orientation of the emitter molecules. From the results the directional characteristics the p-, s- or un-polarised emission can be analysed. Apart from that it is also possible to gain information about emission ratio, that take place in the different channels like described in section 2.4.

4 Results and Discussion

4.1 Differences between neat DBP and DIP films

First the results from the characterisation of the thin films shall be discussed. As said before the difference in the chemical structure between the DBP and the DIP molecule is very small. In order to get access to more information about the morphology of the films the absorption coefficients are determined, AFM images are taken, XRD scans were performed and the angle-resolved spectra of the PL and the outcoupled SPP are measured.

Figure 4.1 shows the difference in absorption between the two molecules. 50 nm of both materials were deposited on a glass substrate and measured by a reflectometer. The absorption coefficient α was calculated using Eq. 3.1 and plotted as a function of the wavelength.

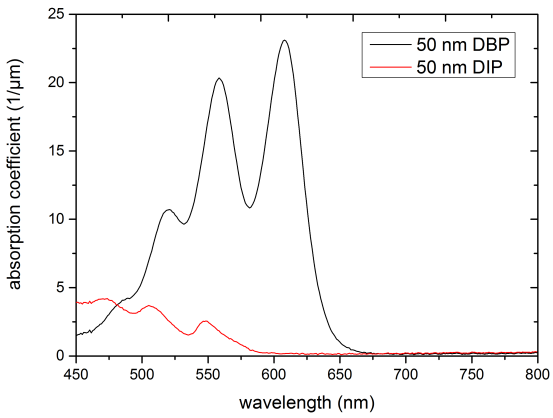

Figure 4.1: Absorption coefficient of DBP and DIP, measured at 50 nm thick layers.

The difference in terms of absorption between the two molecules is remarkable. For instance at a constant wavelength of 550 nm the DBP molecules absorb 7 times more light than the DIP molecules. The obtained results are in good agreement with the literature in the case of the DBP layer [35] and in case of the DIP layer [17]. A possible explanation of the higher absorption of the DBP molecules can be explained by their growth orientation.

In order to determine the influence of the HTL as a substrate for the growth of DIP and DBP 30 nm thin films of α-NPD were deposited on a glass substrate followed by the deposition of 20 nm DIP and DBP respectively. The results obtained after the determination of the absorption coefficients can be seen in Fig. 4.2.

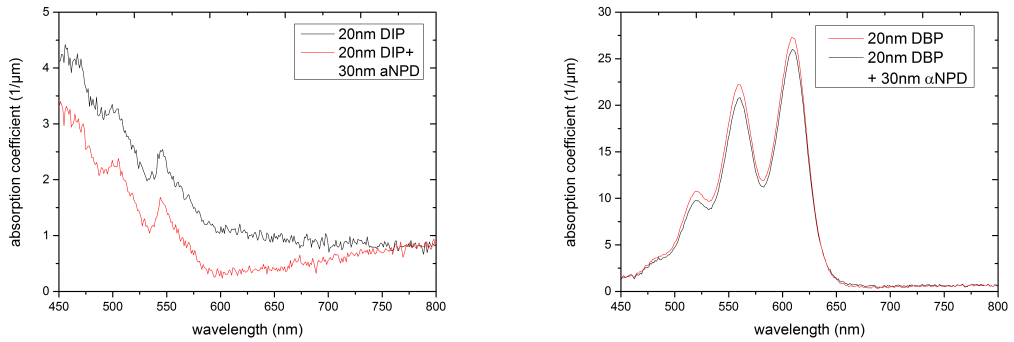

(a) DBP (b) DIP

Figure 4.2: Absorption coefficient measured of a 20 nm thick DIP (a) and DBP layer (b) deposited onto 30 nm of α-NPD. The absorption coefficient determined of a 20 nm thick layer of DIP and DBP is also drawn.

In the case of DIP deposited onto α-NPD the double-layer exhibit a higher absorption coefficient compared to the single layer over the complete wavelength range. But the individual DIP peaks appear at the same wavelength. In the case of the DBP layers the double-layer show an absorption coefficient that is a little bit smaller, than α of the pure DBP layer. The aberrations are possibly due to small variations in the thickness of the glass substrate and the DBP and DIP layers.
In general it can be said that the absorption of the EML changes only slightly if it is deposited onto the HTL or in other words the growth process can be assumed to be not very different.

Apart from that also 30 nm thick layers of DIP and DBP with a substrate temperature of 87°C during deposition were produced. This temperature was selected, because later on also OLEDs at this substrate temperature were produced. But in this case the substrate consisted of glass, ITO, PEDOT:PSS and α-NPD. Since the last material was directly heated it had to be ensured, that this HTL will not be crystallise and expand, because its electronic properties and consequently the properties of the hole device would otherwise decrease dramatically [36]. The glass transition temperatures of α-NPD vary in the literature between 95°C [37] and 100°C [25]. The absorption coefficients of these layers, in comparison to the layers produced at room temperature (RT), are displayed in Fig. 4.3.

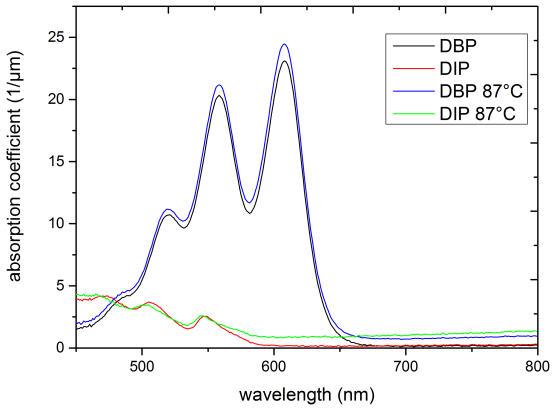

Figure 4.3: Absorption coefficient of measured of 30 nm thick layers of DBP and DIP created at a substrate temperature of 87°C. The absorption coefficient determined of a 20 nm thick layer of DBP and DIP produced at room temperature are also drawn.

It can be seen that the absorption is measured to be a little bit higher for the heated DBP film compared to the RT film. In the case of the DIP films no clear difference between the two films are visible. In general it can be said, that the DBP films absorb way stronger within the visible region of the electromagnetic spectrum than the DIP films. This result could lead to the proposal, that the DBP molecules exhibit a rather horizontal and the DIP molecules a rather vertical orientation within neat films. But further investigations with the help of an AFM and especially with measurements of the p-polarised angle-dependent PL of thin films are necessary to confirm this proposal.

The technique of XRD was used to receive information about the crystallinity of the already presented single and double-layers of DIP and DBP with or without α-NPD. Fig. 4.4 shows a section of this scan.

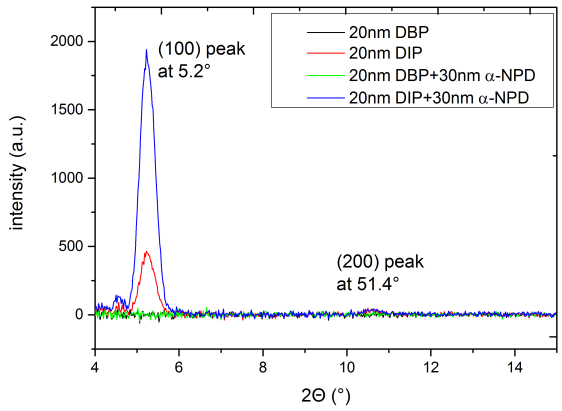

Figure 4.4: XRD diffractogram of 20 nm thin DIP/DBP single and double layers with 30 nm thick α-NPD substrate. The DIP films exhibit polycrystalline behaviour (peaks at 5.2 and 51.4 °) while the DBP films only show an amorphous phase.

The obtained results reveal that the DBP films show no peaks within the diffractorgram and exhibit consequently an amorphous phase. The DIP films, on the contrary, show a crystalline phase. The (100) peak at 5.2 ° is clearly and the (200) peak at 51.4 ° is weakly visible. The obtained results are in good agreement with the reported sigma-phase of DIP showing a standing orientation of the molecules [17]. It is noteworthy, that the (100) peak of the DIP double-layer is more intense, but the value of the full width half maximum is 0.423, which is only slightly greater than the value for the DIP peak (0.417). This could lead to the conclusion that DIP exhibit the same crystallinity if deposited onto glass or on α-NPD.

The method of AFM was used to obtain information about the morphology on the top surface of the two different layers. 20 nm of both materials were deposited onto a glass substrate and measured along the y-direction. All obtained images were treated with the software Gwyddyon and show an area of 2x2 µm. First, images of the surface of 20 nm thick DBP and DIP films are illustrated in Fig. 4.5.

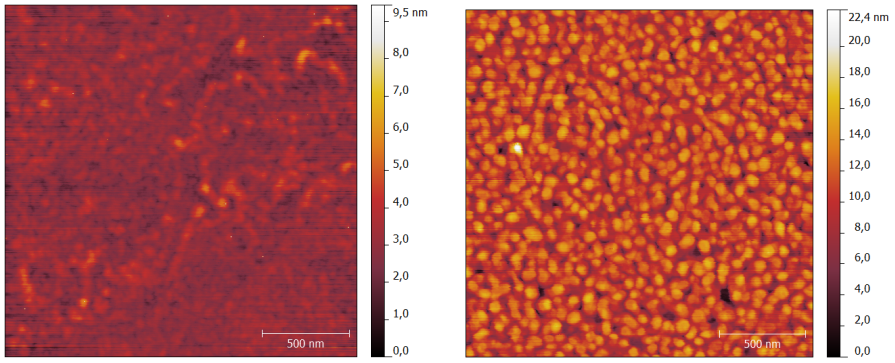

(a) DBP (b) DIP

Figure 4.5: AFM images of 20 nm thin layers of DBP (a) and DIP (b).

The images reveal, that the DBP film exhibit a rather smooth surface, while in the case of the DIP films small crystallites are clearly visible. With the help of Gwyddyon also values for the roughness of the surfaces can be determined. A route-mean-square (rms) value of 0.54 nm was measured for the DBP layer and 2.42 nm for the DIP layer. These values confirm the subjective impression of the morphology.

Apart from that also AFM images of the double-layers 20 nm DBP and DIP deposited onto 30 nm of α-NPD were obtained (Fig. 4.6). The roughness rms values were determined to be 0.97 nm for the DBP double-layer and 2.12 nm for the DIP double-layer. Compared with the images and rms values of the single layers it can be said, that the growth process of DBP onto the HTL is changed to a little bit rougher surface, while DIP is growing in the way that the final surface appears to be smoother.

Fig. 4.7 shows an AFM image of a 30 nm thick layer of α-NPD. It can be seen that the surface of this HTL is also smooth with an rms value of 1.1 nm. The small white spots are so called artefacts of the AFM device.

The obtained AFM images of the 30 nm thick layers of DBP and DIP processed at 87°C can be seen in Fig. 4.8. From the figure and from the rms value of 0.79 nm it can be concluded, that the DBP surface is getting a little bit rougher if it is deposited at elevated temperatures. Also the image of the DIP layer reveal, that the crystallites are growing

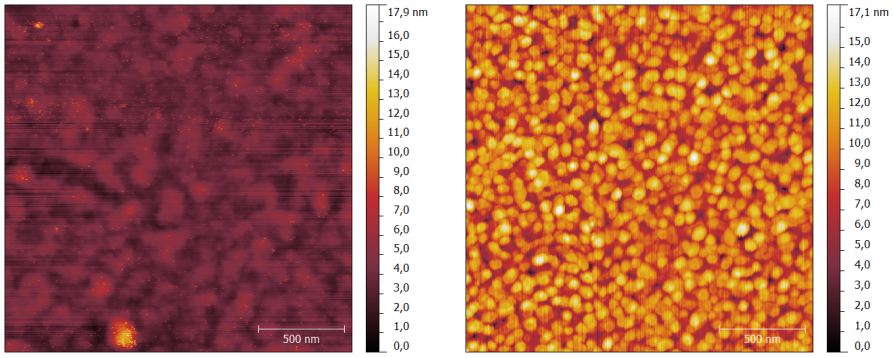

(a) DBP+α-NPD (b) DIP+α-NPD

Figure 4.6: AFM images of 20 nm thin layers of DBP (a) and DIP (b) deposited onto 30 nm α-NPD.

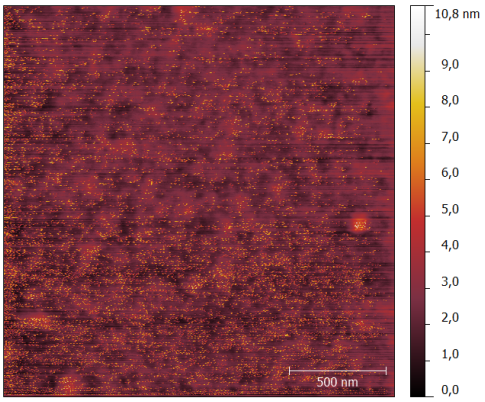

Figure 4.7: AFM images of 30 nm thin layer of α-NPD.

bigger even though the rms value of 2.34 nm is almost the same like the one from the room temperature sample (2.42 nm).

The presented method of angle-resolved PL was used to obtain information about the orientation of the molecules within 30 nm thick films of DBP and DIP deposited onto a glass substrate. The obtained p-polarized spectra in the angle range from 0 to 90 ° can be seen in Fig. 4.9 (a). Fig. 4.9 (b) shows the simulated PL spectrum.

Apart from the fact, that the measured spectrum exhibit a lower PL intensity the shape of the two spectra is similar. The intensity of the simulated spectrum was normalised

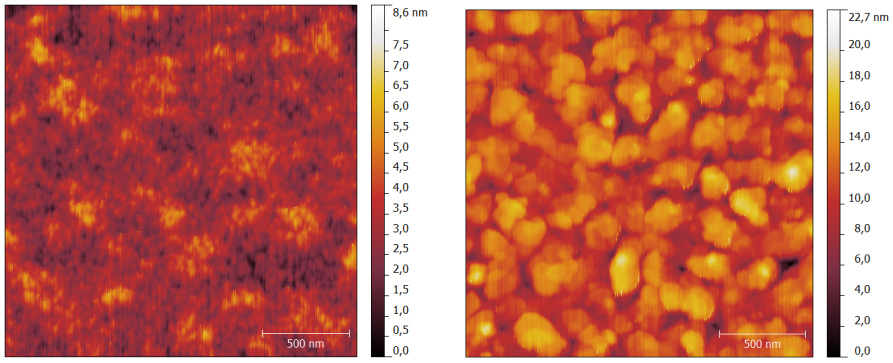

(a) DBP@87 °C (b) DIP@87 °C

Figure 4.8: AFM images of 30 nm thick layers of DBP (a) and DIP (b) produced at a substrate temperature of 87°C.

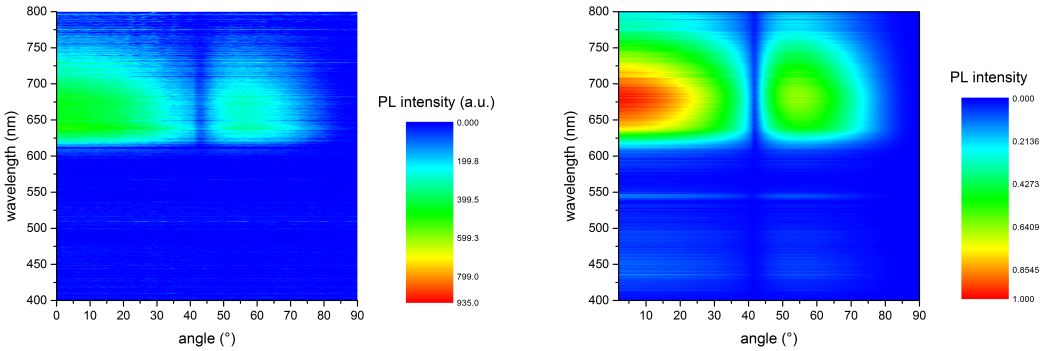

(a) measured spectrum (b) simulated spectrum

Figure 4.9: Angle-resolved p-polarised PL spectrum of a 30 nm thick DBP film (a) and the corresponding simulated spectrum with extraordinary optical constants and a distribution of dipoles p_x- p_y- and p_z in the ratio 1:1:0.1(b).

to the maximum. Both spectra show a rather broad emission with a peak intensity at 660 nm. If a cut is performed at this wavelength Fig. 4.10 is obtained. The intensity was normalised to the value at 0°. The measured cross-section is displayed as a black line. The simulated cross-section in the case of an isotropic dipole orientation, that means the p_x- and p_z-dipoles are present in the same amount in the film, is illustrated as a blue line. It can be seen, that the measured cross-section differs greatly from this dipole distribution. If the amount of p_z is selected to be 0.1 a good agreement between the measured and

the simulated cross-section could be found. This setting was also used for the simulation of the complete angle-resolved PL spectrum of Fig. 4.9 (b). This amount of p_z-dipoles corresponds to a ratio of 4.8 % vertical dipoles. Therefore the orientation of the molecules within a pure DBP layer can be assumed to be almost fully horizontal.

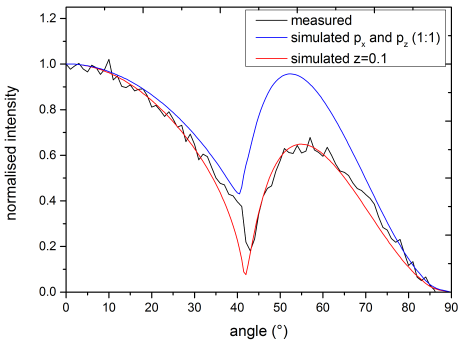

Figure 4.10: Measured and simulated result of a cross-section at 660 nm of the p-polarised PL spectrum of a 30 nm thick DBP layer.

It is noteworthy, that for the performed simulations the extraordinary optical constants of a DBP layer was used. DBP shows birefringence due to its anisotropic growth. The ordinary (subscript o) and extraordinary (subscript e) refractive coefficient n and extinction coefficient k of DBP were extracted from the publication of Yokoyama *et al.* [38] and are shown in Fig. 4.11. It can be seen, that the birefringence lead to different optical constants within the thin film plane (subscript o) and perpendicular to it (subscript e).

It also has to be mentioned, that this birefringence of DBP can not be taken into account in the simulation software. Because only either the ordinary optical constants or the extraordinary optical constants can be implemented. This is also the reason, why the performed simulation with a p_y-ratio of 1 simulated with the extraordinary optical constants (n_e, k_e) drawn as the red line, does not agree very well with a performed cut at 660 nm of the s-polarised PL spectrum displayed as the black line in Fig. 4.12. The PL emission profile that was obtained after a simulation with the ordinary optical constants (n_o, k_o) is shown as a green line. This profile shows an even greater aberration to the measured profile. To simulate the trend of the measured curve it would be necessary to implement the birefringence within the simulation software.

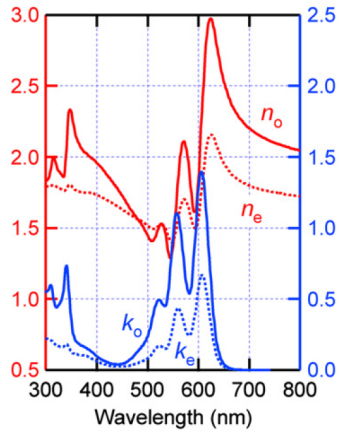

Figure 4.11: Ordinary (subscript o) and extraordinary (subscript e) refractive coefficient n and extinction coefficient k of DBP, extracted from the publication of Yokoyama *et al.* [38]

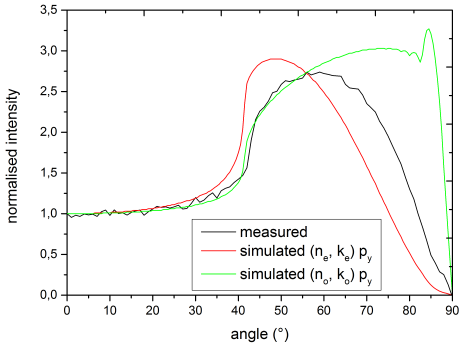

Figure 4.12: Measured and simulated result of a cross-section at 660 nm of the s-polarised PL spectrum of a 30 nm thick DBP layer.

Now the results of the p-polarised PL measurement of a 30 nm thick neat DIP film shall be discussed. The measured and simulated spectra are illustrated in Fig. 4.13. Apart from the lower intensity of the measured spectrum the qualitative shape of the p-polarised PL signal of the measured and simulated spectrum is the same. Both show a broad emission with the maximum intensity at 680 nm. Fig. 4.14 shows the cross-section at this wavelength.

From Fig. 4.14 it can be seen, that the cross-section of the measured signal (black line) shows a higher intensity at an angle of 50° compared to a cross-section from the simulated

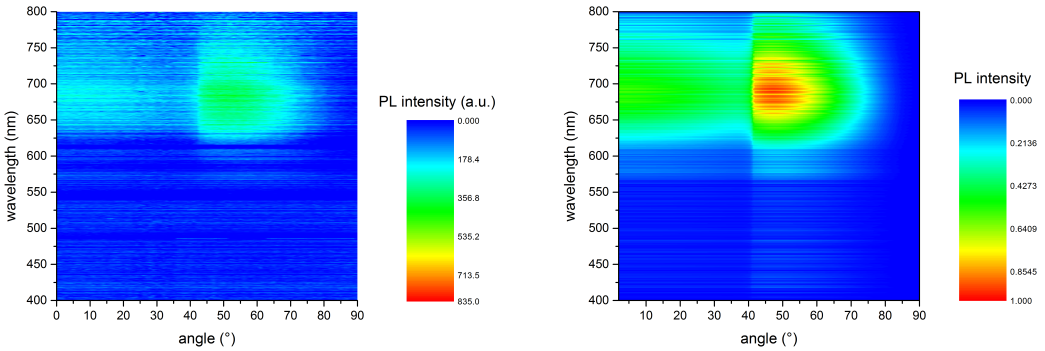

(a) measured spectrum (b) simulated spectrum

Figure 4.13: Angle-resolved p-polarized PL spectrum of a 30 nm thick DIP film (a) and the corresponding simulated spectrum with a distribution of dipoles p_x- p_y- and p_z in the ratio 1:1:2.2 (b).

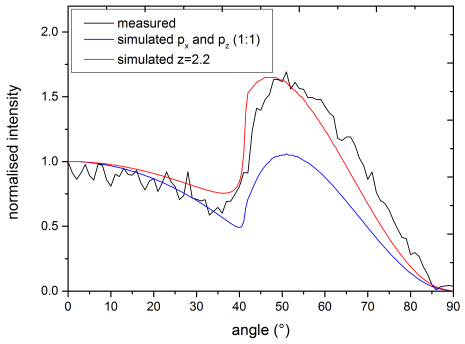

Figure 4.14: Measured and simulated result of a cross-section at 680 nm of the p-polarised PL spectrum of a 30 nm thick DIP layer.

spectrum, where an isotropic dipole orientation is assumed (blue line). If the amount of p_z-dipoles was set to be 2.2 the simulated cross-section (red line) agrees quite good with the measured data. This setting was also used for the simulation of the complete angle-resolved PL spectrum of Fig. 4.13 (b). This distribution of the transition dipoles correlates to an amount of 52 % vertical dipoles. Consequently it can be said, that the molecules show a rather vertical orientation.

A cross-cut of a measured (black line) and simulated (red line) s-polarised spectrum at 680 nm with a ratio of p_y of 1 can be seen in Fig. 4.15. A good agreement between the measured and simulated cross-section is visible.

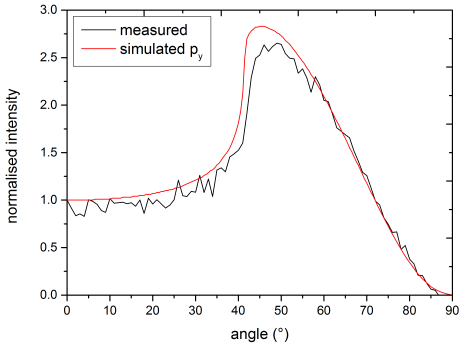

Figure 4.15: Measured and simulated result of a cross-section at 680 nm of the s-polarised PL spectrum of a 30 nm thick DIP layer.

In addition to the presented results until now also 30 nm thick samples of DBP and DIP while the glass substrate was heated to a temperature of 87°C during deposition of the perylene layers were analysed by angle-resolved PL measurements.
First the effect of the elevated substrate temperature on the growth conditions of the DBP molecules shall be examined. After a cut of the p-polarised spectra was performed at 660 nm Fig. 4.16 is obtained.

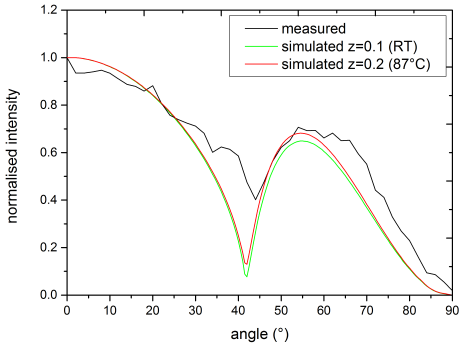

Figure 4.16: Measured and simulated result of a cross-section at 660 nm of the p-polarised PL spectrum of a 30 nm thick heated DBP layer.

From the figure it can be concluded, that the selected p_z-dipole fraction of 0.1, that was selected to describe the measurement result of the DBP film produced at room temperature, is not adequate to the describe the measured cross-section. If the p_z-dipole fraction is increased to a value of 0.2 the agreement between the measured and simulated result is quite good. This ratio of the p_z-dipoles corresponds to an amount of 9 % vertical dipoles that are now present in the DBP film. Consequently, it can be said, that the elevated temperature lead to a loss in ordering of the molecules within the DBP film.

At this point the results from the angle-dependent PL measurement of the heated DIP film shall be discussed. The cross-section at 680 nm of the p-polarised PL spectrum and the results of the performed simulations are summarised in Fig. 4.17.

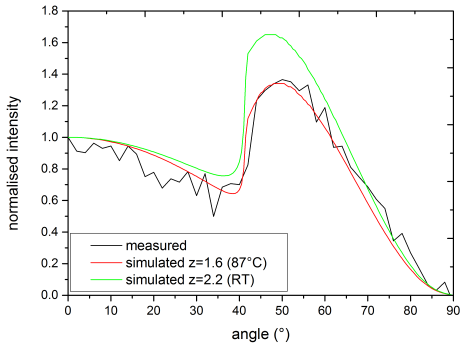

Figure 4.17: Measured and simulated result of a cross-section at 680 nm of the p-polarised PL spectrum of a 30 nm thick heated DIP layer.

In the case of heated substrate during deposition of the DIP molecules it comes to a decrease of the p_z-dipole fraction from 2.2 at room temperature to a value of 1.6 at 87°C. The amount of vertical dipoles decreased from 52 % to 44 %. This result could lead to the statement, that the orientation of the DIP molecules goes towards an isotropic orientation at elevated substrate temperatures.

In order to determine the coupling strength of the DBP and DIP molecules to SPP a 35 nm thick Ag layer that was deposited onto a glass substrate was used as a substrate for the deposition of 35 nm of DBP and DIP, respectively. The measured spectra are normalised to the PL emission of the corresponding layers at an angle of 180° (Fig. 4.18). This is

necessary to compare the detected signals from the SPPs of the DBP and DIP layers, because both materials may exhibit different values of the effective radiative quantum efficiency q_{eff}.

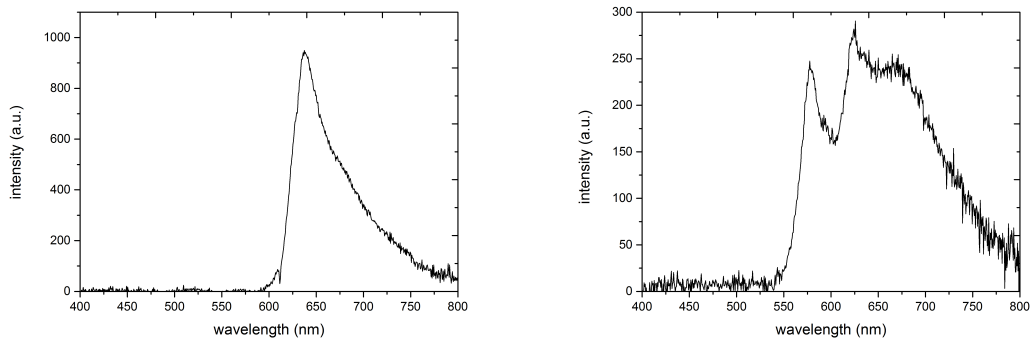

(a) DBP PL spectrum

(b) DIP PL spectrum

Figure 4.18: PL spectra of the layer system 35 nm DBP+35 nm Ag (a) and 35 nm DIP+35 nm Ag (b). Both spectra were obtained after a measurement at an angle of 180 °.

While the DBP film shows a rather sharp and intense PL signal at 640 nm, the signal from the DIP film is weak and broad with two main peaks at 575 and 645 nm. The measured and simulated SPP spectra of the DBP stack can be seen in Fig. 4.19. For the simulation of the spectrum the results of the angle-dependent PL measurement of the DBP film were used.

The simulated SPP spectrum agrees quite good with the measured spectrum. Possible aberrations are do to the fact, that also for this simulation the birefringence of the DBP film could not be taken into account. The assumption with the same ratio of transition dipole moments like determined from the angle-resolved PL measurements could also lead to differences, because in this case the organic layers were deposited onto a silver and not onto a glass substrate. The same explanations can be applied to the difference in measured and simulated spectra of the DIP film (Fig. 4.20).

Nevertheless a statement can be made to the coupling strength of both perylene based materials. If the maximum intensity values of both spectra are compared it can be said, that the DIP molecules couple way stronger to SPP (value 0.0328) compared to the DBP molecules (value 0.00267). The difference is one order of magnitude and was expected

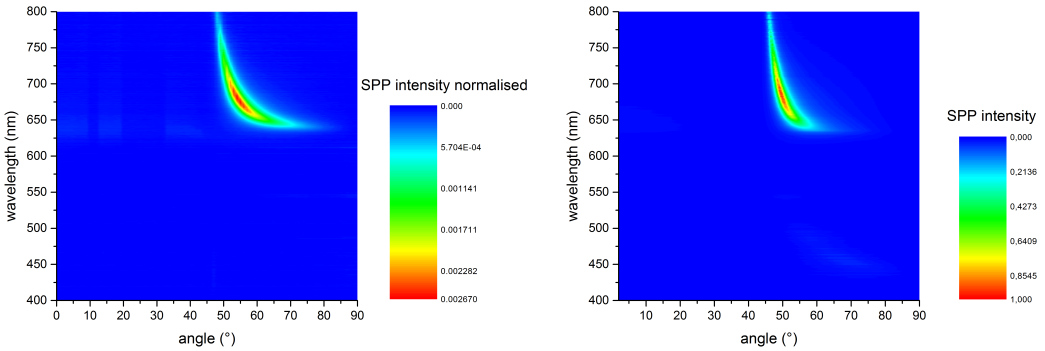

(a) measured spectrum

(b) simulated spectrum

Figure 4.19: Spectra of the outcoupled SPP signal of a layer system of 35 nm DBP deposited onto 35 nm Ag. The measured spectrum are normalised to the PL emission of the corresponding layer (Fig. 4.18 (a)). The simulated spectrum is obtained for a DBP thickness of 35 nm.

since the DIP molecules exhibit a rather vertical orientation with a p_z-dipole ratio of 2.2, while the DBP molecule show a horizontal orientation (p_z-dipole ratio 0.1).

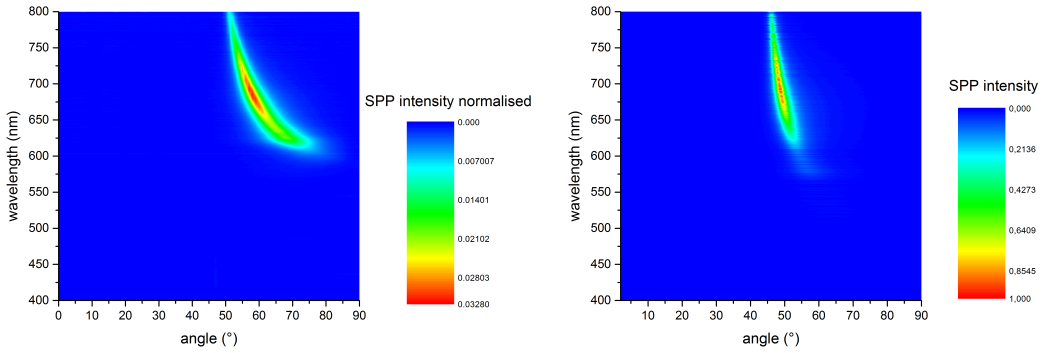

(a) measured spectrum (b) simulated spectrum

Figure 4.20: Spectra of the outcoupled SPP signal of a layer system of 35 nm DIP deposited onto 35 nm Ag. The measured spectrum are normalised to the PL emission of the corresponding layer (Fig. 4.18 (b)). The simulated spectrum is obtained for a DIP thickness of 35 nm.

4.2 Differences between rubrene films doped with DBP or DIP

In this section the results of the characterisation of the doped DIP and DBP films shall be presented. 1 % of the two different perylene materials were doped into rubrene as the host material. 15 nm thick films of these doped films were analysed using the method of angle-dependent PL. The measured and simulated p-polarised spectra of the doped DBP can be seen in Fig. 4.21.

It can be said, that there is a good agreement between the measured and simulated p-polarised spectra. The spectra show two well defined peaks at 610 and 660 nm. In order to characterise the obtained spectra further a cut was performed at a wavelength of 610 nm (Fig. 4.22 (a)). It can be seen, that the orientation of the dipoles differ greatly from an isotropic orientation. If it is selected in the simulation, that no p_z-dipoles are present in this film there is a good agreement between the measured and simulated curve. This result lead to the conclusion, that the DBP molecule show a complete horizontal orientation if they are dissolved within the rubrene matrix.

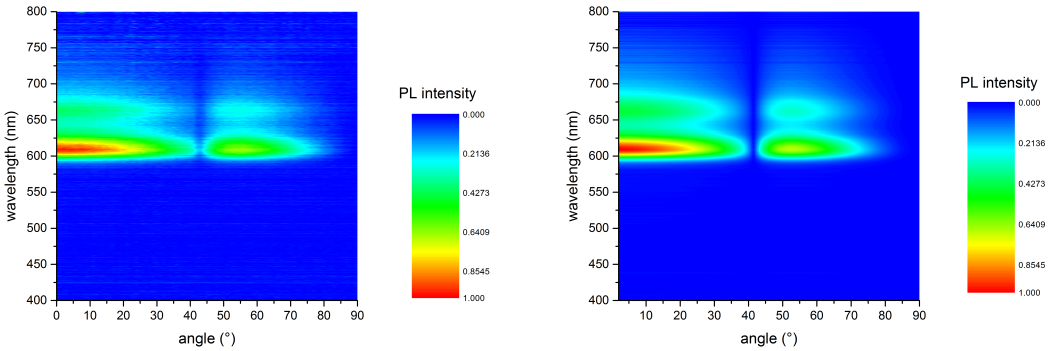

(a) measured spectrum (b) simulated spectrum

Figure 4.21: Measured (a) and simulated angle-resolved PL p-polarised spectra (b) of a 15 nm thick 1 % DBP:Rubrene film. For the simulated spectrum a distribution of dipoles p_x- p_y- and p_z in the ratio 1:1:0 was selected.

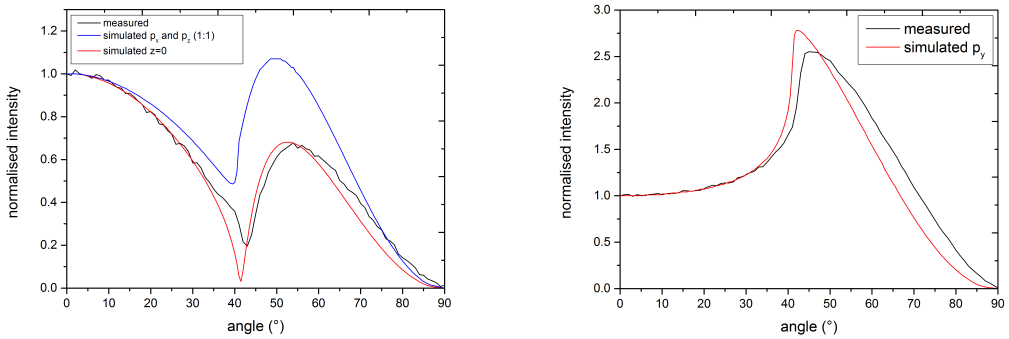

(a) measured spectrum (b) simulated spectrum

Figure 4.22: Measured and simulated results of a cross-section at 610 nm of the p- (a) and s-polarised PL spectrum (b) of a 15 nm thick 1 % DBP:Rubrene layer.

In order to check if the results of the p-polarised PL measurements are correct also a cut at 610 nm of a s-polarised PL spectrum is investigated. The cross-cut can be seen in Fig. 4.22 (b). It shows a quite good agreement between the measured and simulated curve of the p_y-dipoles. These results reveal, that the DBP molecules exhibit a horizontal orientation in the neat and also in the doped films.

Now the results of the angle-dependent p-polarised PL measurements of a 15 nm thick layer of 1 % DIP that was doped into rubrene shall be presented and discussed. Fig. 4.23 illustrates the measured and simulated p-polarised spectra of this layer.

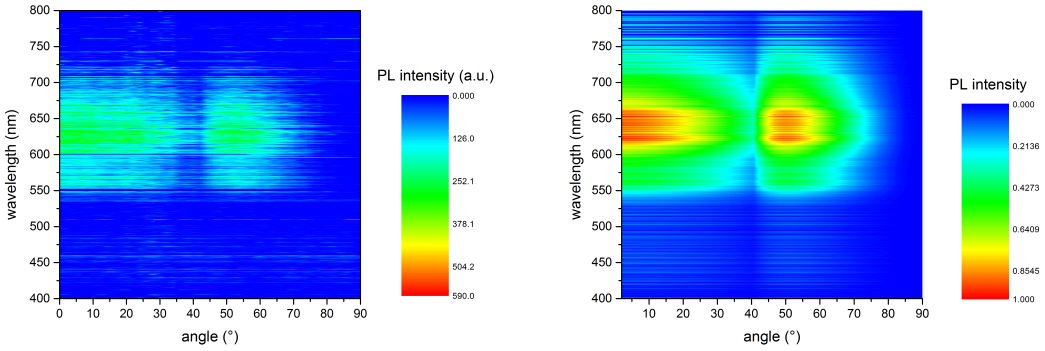

(a) measured spectrum

(b) simulated spectrum

Figure 4.23: Measured (a) and simulated angle-resolved PL p-polarized spectra (b) of a 15 nm thick 1 % DIP:Rubrene layer. For the simulated spectrum a distribution of dipoles p_x- p_y- and p_z in the ratio 1:1:0.6 was selected.

It can be seen, that apart from the low intensity of the measured spectrum, the agreement between the measured and simulated spectra is good. The emission of this doped layer is rather broad with a peak intensity at around 640 nm. If a cut at this wavelength is performed Fig. 4.24 (a) is obtained. Also the DIP molecules differ from an isotropic dipole orientation (blue line) if they are dissolved into rubrene. If a z-value of 0.6 is selected for the simulation (red line) the trend is close to the measured cross-section (black line). This ratio of the p_z-dipoles corresponds to an amount of 23 % vertical dipoles. This value is a lot smaller than the value at the neat DIP film with an amount of 44 % and could lead to the conclusion that the DIP molecules are oriented more isotropic if they are dissolved inside a matrix.

The cross-section of the measured and simulated s-polarised spectra can be seen in Fig. 4.24 (b). The differences are small and it can be said, that the optical constants that were used for the simulations are correct.

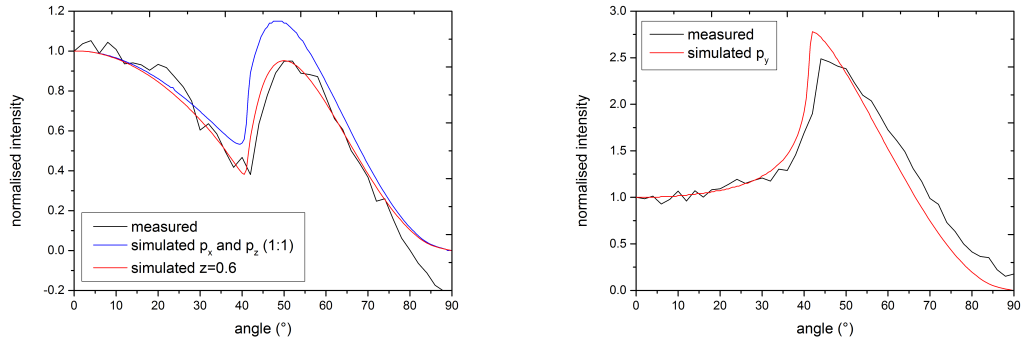

(a) measured spectrum

(b) simulated spectrum

Figure 4.24: Measured and simulated results of a cross-section at 640 nm of the p- (a) and s-polarised PL spectrum (b) of a 15 nm thick 1 % DIP:Rubrene layer.

4.3 Differences between neat DBP and DIP OLEDs

In this section the differences in the produced OLEDs with DBP or DIP as the material for the EML shall be discussed. First images of the operated OLEDs and their measured voltage-dependent EL spectra are presented. Then the J-V-L curves and the EQE of each device are displayed and discussed. The effect of heating the substrate before and during the depostion of DBP and DIP as the EML of the analysed OLEDs is also investigated and compared to the results from the OLEDs produced at room temperature. Apart from that the angle-resolved un-polarised EL emission spectra from the RT OLEDs are presented and compared with performed simulations.

If all four pixels of the two different OLEDs are powered with a voltage of 6 V in the case of the DBP and 7 V in the case of the DIP OLEDs, the two images 4.25 (a) and 4.26 (a) can be obtained. Their corresponding voltage dependent EL spectra at 0° are attached too (Fig. 4.25 (b) and Fig. 4.26 (b)).

Fig. 4.25 (b) shows, that the red DBP OLED exhibits a peak intensity at a wavelength of 670 nm. The peak is asymmetric and shows a shoulder at 640 nm. The emission profile also does not change at a high operating voltage of 8 V. Included into the figure is the stack of the analysed OLED. The orange DIP OLED with a peak intensity at 680 nm

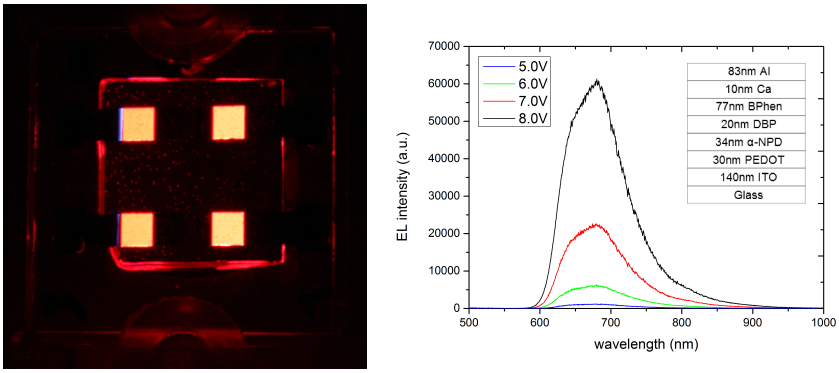

(a) DBP OLED (b) EL spectra

Figure 4.25: Image of the powered DBP OLED at 6 V a) and their voltage dependent EL spectra b) showing a maximum of intensity at a wavelength of around 670 nm.

shows a symmetric emission peak. A small second peak at a wavelength of 580 nm is also visible. The emission profile does not change even at very high operating voltage of 10 V.

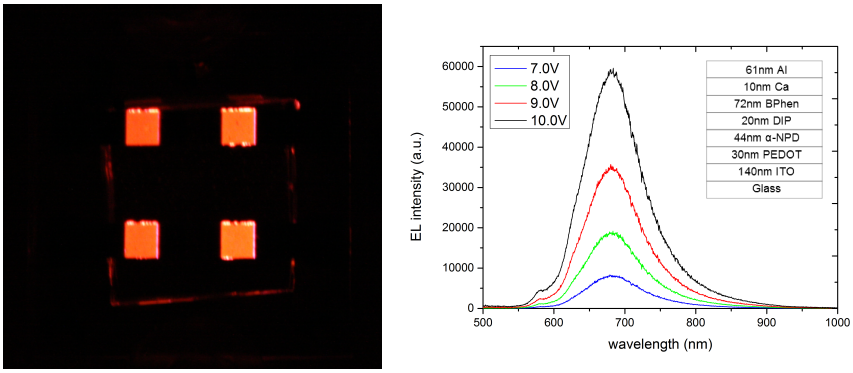

(a) DIP OLED (b) EL spectra

Figure 4.26: Image of the powered DIP OLED at 7 V a) and their voltage dependent EL spectra b) showing a maximum of intensity at a wavelength of around 680 nm.

Now the results of the electronic characterisation of the produced OLEDs are discussed. In order to compare the obtained results the corresponding stack of the analysed OLEDs containing the different thickness values of the various layers are inserted in each figure. This is important because the thickness of the layers especially of the ETL and HTL has a major effect on the outcoupling efficiency like already discussed in section 3.1.
The *J*-*V*-*L*-curve of one pixel of the two different OLEDs are shown in Fig. 4.27. The

black curves from the DBP OLED show a slightly lower value for the leakage current density but a stronger signal for the luminance compared to the DIP OLED. The values for L at a operating voltage of 6 V were measured to be 8 cd/m^2 for the DBP and around 1 cd/m^2 for the DIP OLED. The built-in voltage for the DIP OLED is around 2.4 V, which is slightly lower than the built-in voltage of the DBP OLED with 2.8 V.

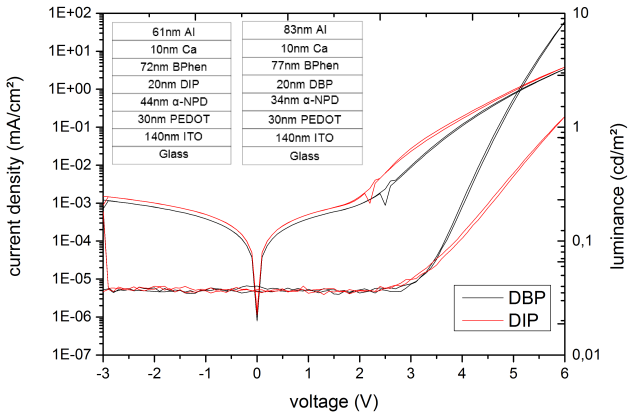

Figure 4.27: J-VL-curve of one pixel of an OLED comprising DBP (black curves) and DIP (red curves) as the EML. The DBP OLED exhibit a little smaller amount of leakage current and a higher luminance compared to the DIP OLED.

The result of the EQE measurement of the DBP and DIP OLEDs are displayed in Fig. 4.28 (a) and Fig. 4.28 (b), respectively. It can be seen, that the values of the DBP OLED pixels (0.2 %) are five times larger than the values of the DIP OLED pixels (0.04 %). The almost horizontal trend of the EQE curves in the case of the DIP OLEDs show that the charge carrier balance is quite good. The peak trend in the case of the DBP OLED is a hint for a imbalance of charge carriers. The reason for this effect is the shift in injection barriers at the cathode and anode and the change in the recombination site [39]. The differences in dipole orientation between the DBP molecules and the DIP molecules contribute to this huge difference in efficiency. The other factor that may explain this difference is the effective radiative quantum efficiency of the two OLEDs. q_{eff} could be very different in the DBP and the DIP OLED. This important factor should be determined for both OLEDs to really make a statement of how much the dipole orientation contribute to the efficiency increase.

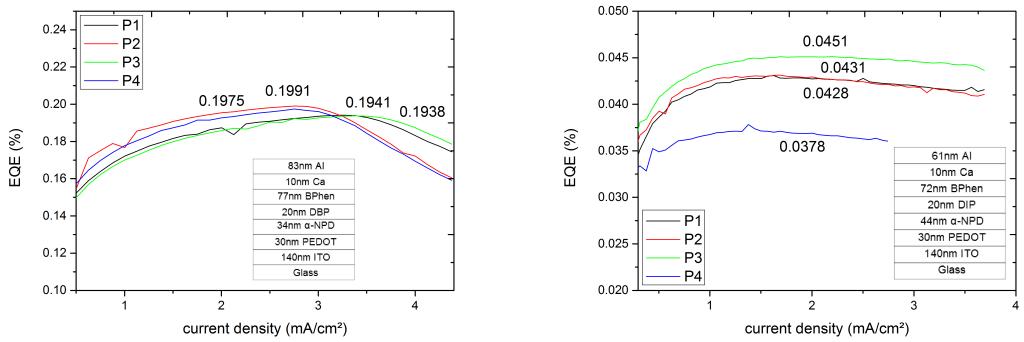

(a) DBP RT

(b) DIP RT

Figure 4.28: Results of the EQE measurement for all four pixels of the DBP OLED (a) and DIP OLED (b) produced at room temperature. The indicated values for the EQE describe the maxima of the four different pixels P1 to P4. The analysed OLED stack is also included.

In order to determine the effect of the substrate temperature during deposition of the two different EML on the OLED performance, four different OLEDs were produced. The first two OLEDs were produced in the way, that the substrate was heated to a temperature of 87 °C during the deposition of DBP and DIP. These OLEDs were labeled as DBP EML 87°C and DIP EML 87°C. In the case of the other two OLEDs only the stack comprising the glass substrate, the structured ITO layer the PEDOT:PSS layer and the α-NPD layer was heated to a temperature of 87 °C for 20 minutes. The deposition of DBP and DIP was performed at room temperature like in the OLEDs presented so far. These OLEDs were labelled as DBP HTL 87°C and DIP HTL 87°C. First the results from these two OLEDs shall be discussed.
Fig. 4.29 displays the J-V-L-curves of the DBP and DIP OLEDs, where the HTL was heated. Both OLEDs exhibit the same value for the leakage current density and the built-in voltages are the same compared to the RT OLEDs. But the DBP OLED show a stronger luminance efficiency at 6 V with a value of 17 cd/m^2 compared to a value of 2 cd/m^2 for the DIP OLED.

The results of the EQE measurements of the DBP and DIP OLEDs where the HTL was heated are shown in Fig. 4.30. The values with 0.14 % in the case of the DBP are lower compared to the OLEDs where the HTL was not heated prior to the deposition of DBP. In the case of the DIP HTL 87°C OLED the EQE values were measured to be almost

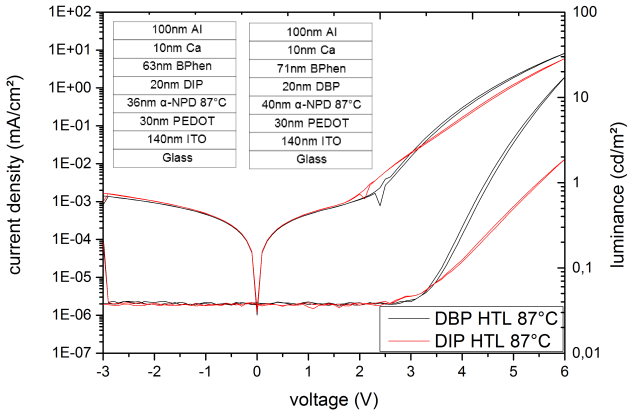

Figure 4.29: J-V-L-curve of one pixel of an OLED comprising DBP (black curves) and DIP (red curves) as the EML. In this case the HTL was heated to a temperature of 87°C before the DBP and DIP-layer was deposited.

the same than the values from the room temperature OLED. The curves of the EQE measurement has shown the same trend than the curves of the OLEDs produced at RT. The DIP OLED show a rather horizontal trend while the DBP OLED exhibit a peak trend of the curve. A possible explanation for the decrease in efficiency in the case of the DBP could be, that the heating of the α-NPD layer lead to a further decrease in the charge-carrier balance.

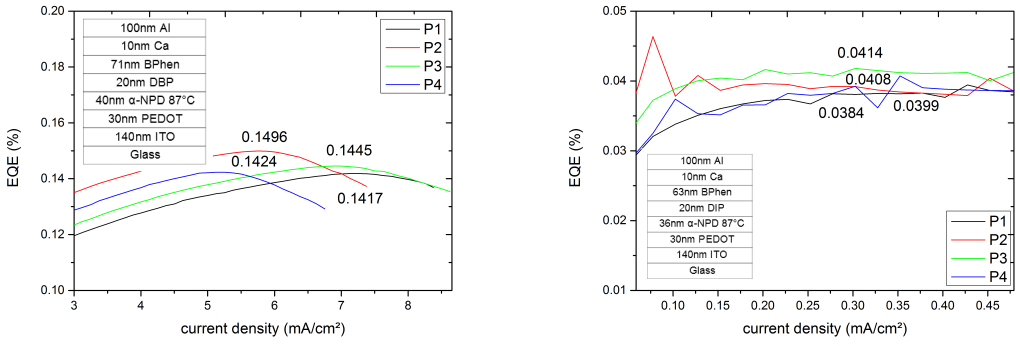

(a) DBP HTL 87°C

(b) DIP HTL 87°C

Figure 4.30: Results of the EQE measurement for all four pixels of the DBP OLED (a) and DIP OLED (b) with heated HTL.

Now the results of the OLEDs where the substrate was heated to a temperature of 87°C during the deposition of the DBP and DIP layers are discussed. It is noteworthy, that also the HTL was heated prior to the deposition of DBP and DIP. Fig. 4.31 shows the *J*-*V*-*L*-curve of DBP (black lines) and DIP OLEDs (red lines) with heated EML. The leakage current density is the same for both OLEDs, but the built-in voltage is 2 V in the case of the DIP OLED and 2.7 V in the case of the DBP OLED. While the value of the DBP OLED is in the same region, than the value of the OLED produced at room temperature or at heated HTL, the value of the DIP OLED is 0.4 V smaller than the values measured at RT or at heated HTL. This can possibly be attributed to an improved charge-carrier injection.

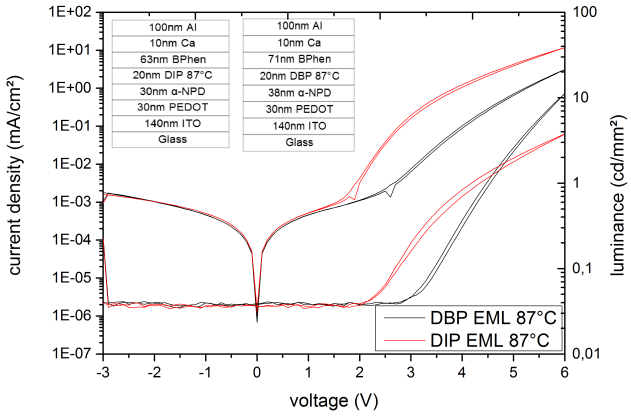

Figure 4.31: *J*-*V*-*L*-curve of one pixel of an OLED comprising DBP (black curves) and DIP (red curves) as the EML. In this case the EML was heated to a temperature of 87°C before the DBP and DIP-layer was deposited.

The results of the EQE measurements of the DBP and DIP OLEDs where the EML was heated are shown in Fig. 4.32. These results reveal, that the heating of the substrate during the deposition of the EML lead to an increase of the EQE values of around 60 % compared to the OLEDs produced without heating the substrate. In comparison to the results of the heated HTL the values could even be doubled for the DBP OLEDs and almost be doubled for the DIP OLEDs. A possible explanation of the increase in efficiency in the case of the DBP OLED could be, that the charge-carrier balance is improved if the DBP layer is deposited onto the heated HTL layer. This can be said, because the trend of the EQE curve in Fig. 4.32 is more horizontal than the peak curves of the results from the RT OLED (Fig. 4.28). This effect exceeds the loss in orientation that could be detected if

the DBP layers was produced at elevated substrate temperature (see Fig. 4.16).
The increase in the EQE values in the case of the heated DIP OLED can be explained by the decrease of the vertical orientation of the dipole molecules, that was detected by angle-resolved PL measurements (see Fig. 4.17). The charge-carrier balance was not improved in this case because all measured EQE curves show the same trend.

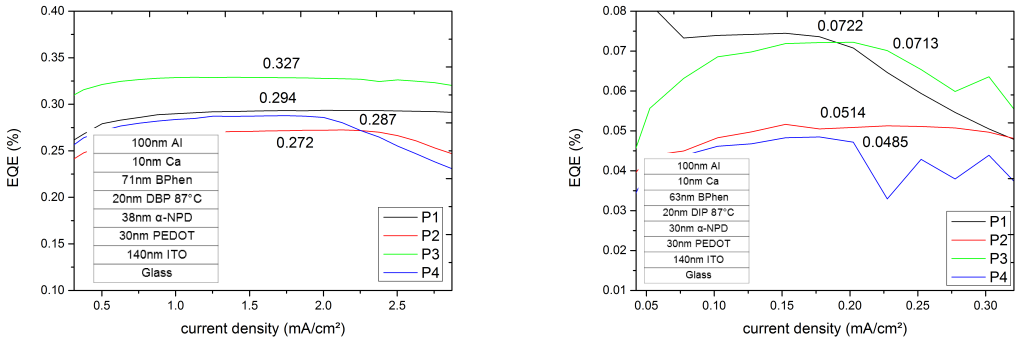

(a) DBP EML 87°C

(b) DIP EML 87°C

Figure 4.32: Results of the EQE measurement for all four pixels of the DBP OLED (a) and DIP OLED (b) with heated EML.

At this point the same RT DBP and DIP OLEDs that were characterised electrically so far shall now be characterised optically. First the obtained results from the un-polarised angle-resolved EL emission spectra of the DBP OLED shall be presented and discussed. The OLED was powered at a voltage of 6 V. The measured and simulated spectra of the DBP OLED if no prism was used to outcouple the substrate modes are displayed in Fig. 4.33. For the simulated spectrum the same dipole distribution (p_x:p_y:p_z 1:1:0.1) than for the angle-resolved PL spectrum from Fig. 4.9 and Fig. 4.10 was used.

It can be seen, that the measured EL spectrum shows a broad emission with a peak intensity at 690 nm with decreasing intensity until an angle of 42°. Also the simulated spectrum shows the same result even tough the intensity of the simulated signal is a lot higher. In order to compare the radiation profile with the profile of a Lambertian radiator a cut at the maximum wavelength at 690 nm was performed (Fig. 4.34). A Lamertian radiator is a radiator where the detected EL intensity does not depend on the viewing angle [5].

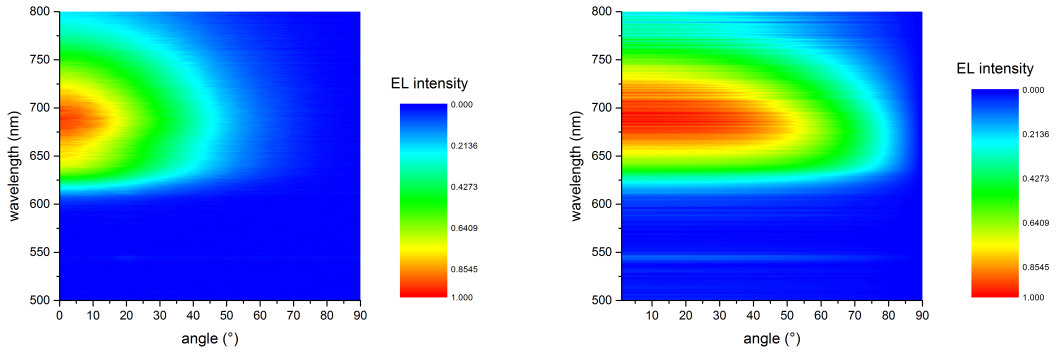

(a) measured spectrum

(b) simulated spectrum

Figure 4.33: Measured and simulated un-polarised angle-resolved EL emission spectra of the DBP OLED from 0° to 90° without the use of a prism.

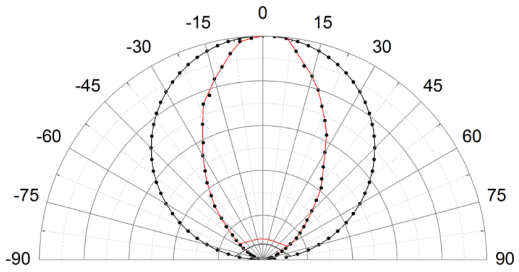

Figure 4.34: Cut of the EL spectrum of the DBP OLED (Fig. 4.33) at a wavelength of 690 nm (red line) compared to the emission profile of a Lambertian radiator (black line) between -90° and 90°.

From Fig. 4.34 it can be seen that there is a huge aberration between the measured emission profile of the DBP OLED (red line) and the emission profile of a Lambertian radiator (black line). It can be said, that the detected intensity is dependent on the viewing angle in the case of the DBP OLED. This result is also illustrated in Fig. 4.35 , that shows a cut at 690 nm of the measured (black line), simulated (blue line) and the spectrum of a Lambertian radiator (red line). The aberrations between measurement and simulation are possibly due to the used optical constants in the simulation.

Now the results of the angle-dependent EL spectra of the DIP OLED shall be discussed. This OLED was powered at a voltage of 7 V since its intensity is smaller than the intensity

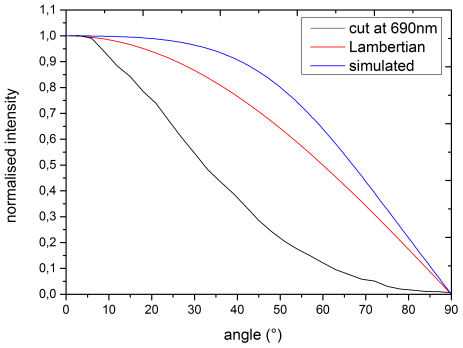

Figure 4.35: Cut of the EL spectrum of the DBP OLED (Fig. 4.33) (black line) and of the corresponding simulated spectrum (blue line) at a wavelength of 690 nm (red line) compared to the emission profile of a Lambertian radiator (red line) between 0° and 90°.

of the DBP OLED. The measured and simulated spectra if no prism was attached to the OLED can be seen in Fig. 4.36. For the simulated spectrum the same dipole distribution (p_x:p_y:p_z 1:1:2.2) than for the angle-resolved PL spectrum from Fig. 4.13 and Fig. 4.14 was used. The simulated spectrum agrees with the measured spectrum. Both show a rather broad emission with a peak intensity at 690 nm that is decreasing towards a larger emission angle.

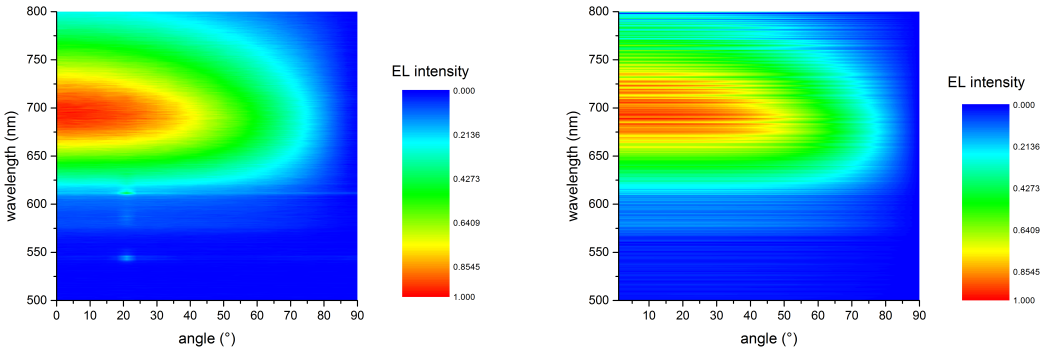

(a) measured spectrum

(b) simulated spectrum

Figure 4.36: Measured and simulated un-polarised angle-resolved EL emission spectra of the DIP OLED from 0° to 90° without the use of a prism.

Fig. 4.37 shows the emission profile at 690 nm. It is in quite good agreement with the emission profile of a Lambertian radiator which corresponds to the orientation of the DIP molecules within the EML that are oriented rather isotropically.

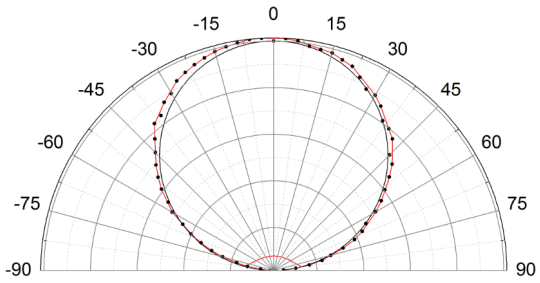

Figure 4.37: Cut of the EL spectrum of the DIP OLED (Fig. 4.36) at a wavelength of 690 nm (red line) compared to the emission profile of a Lambertian radiator (black line) between -90° and 90°.

Fig. 4.38 shows a cut at 690 nm of the measured (black line), simulated (blue line) un-polarised EL emission spectrum of the DIP OLED. Also the emission profile of a Lambertian radiator is included (red line). The emission profile reveal, that the DIP OLED can be characterised as a Lambertian radiator and the simulated profile is quite close to the measurement result. The aberrations between measurement and simulation are possibly due to the used optical constants and the implemented layer thickness values in the simulation.

From the simulation it was also possible to extract the fraction of power that is emitted at the different channels of an OLED like introduced in Fig. 2.4. The result of the simulation of the analysed DBP and DIP OLED produced at RT can be seen in Fig. 4.39.

The DBP OLED emits 27 % of the created light directly to air, while 28 % is trapped in the substrate and 17 % within waveguide modes. 19 % of the power is lost due to the coupling to SPPs and 10 % is absorbed. The DIP OLED emits only 16 % directly to air, 17 % to the substrate, 15 % is lost inside the waveguide mode and the high value of 43 % is lost due to the near-field coupling to SPPs. The remaining 9 % of the dissipated power is lost due to absorption. If a prism is used to outcouple the emission to the substrate 55 % of light can be extracted out of the DBP OLED, while only 33 % can be extracted from the DIP OLED. These results can be connected to the results from the thin film

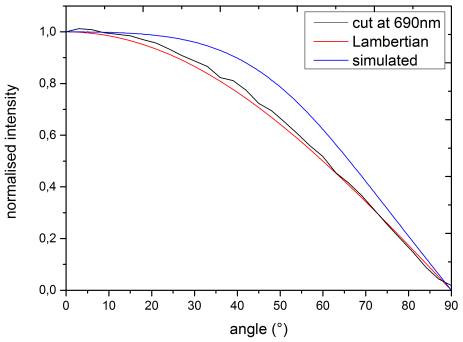

Figure 4.38: Cut of the EL spectrum of the DIP OLED (Fig. 4.36) (black line) and of the corresponding simulated spectrum (blue line) at a wavelength of 690 nm (red line) compared to the emission profile of a Lambertian radiator (red line) between 0° and 90°.

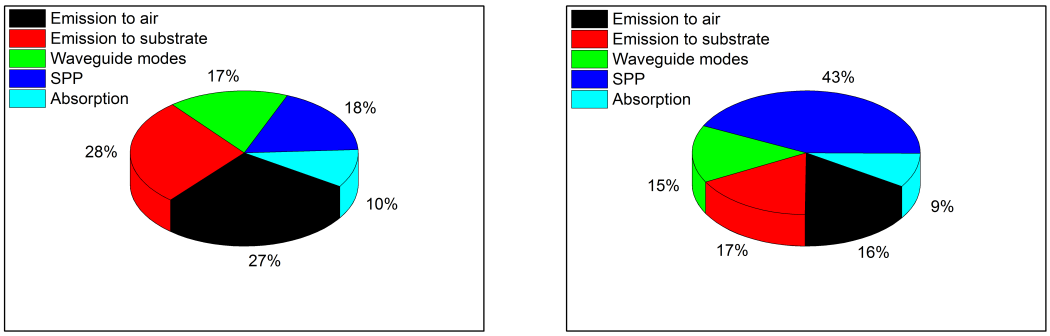

(a) DBP OLED

(b) DIP OLED

Figure 4.39: Ratio of the emitted power into the different optical channels of an OLED in the case of the DBP (a) and DIP OLED (b).

and OLED characterisation, because the DBP EML with the rather horizontal dipole orientation lead to higher EQE values compared to the rather vertical orientation of the DIP EML that can couple strongly to SPP.

4.4 OLEDs with rubrene doped with DBP or DIP as EML

OLEDs comprising an EML of 1 % DBP or DIP doped rubrene were also produced and characterised. The doping concentration was selected to be 1 % because Okumoto *et al.* used the same concentration in their high efficient red DBP:Rubrene OLEDs [27]. The stack of these two OLEDs are displayed in Fig. 4.40. Apart from the thickness of the BPhen layer all layers are equal.

100nm Al
10nm Ca
69nm BPhen
15nm DBP:Rubrene
30nm α-NPD
30nm PEDOT
140nm ITO
Glass

(a) 1 % DBP:Rubrene OLED

100nm Al
10nm Ca
71nm BPhen
15nm DIP:Rubrene
30nm α-NPD
30nm PEDOT
140nm ITO
Glass

(b) 1 % DIP:Rubrene OLED

Figure 4.40: Stack of the analysed 1 % DBP:Rubrene (a) and 1 % DIP:Rubrene OLED (b).

First, images of the operated OLEDs and their corresponding voltage dependent EL spectra are shown. Then the J-V-L and the EQE of each device are displayed and discussed. Finally the angle-dependent EL spectra of both OLEDs are presented. This section closes with a discussion of the simulated results of the emitted power into the different loss channels.

If all four pixels of the 1 % DBP:Rubrene OLED is powered with a voltage of 6 V the image 4.41 (a) can be obtained. Their corresponding voltage dependent EL spectra are attached too (Fig. 4.41 (b)). The spectra of the red OLED show two peak maxima at 610 and 660 nm. Additionally, no spectral peak of the rubrene can be seen even at a high voltage of 9 V. This peak of a pure rubrene emission should normally occur at around 510 nm [40]. The obtained emission spectra is in good agreement with the measured spectrum by Okumoto *et al.* [27].

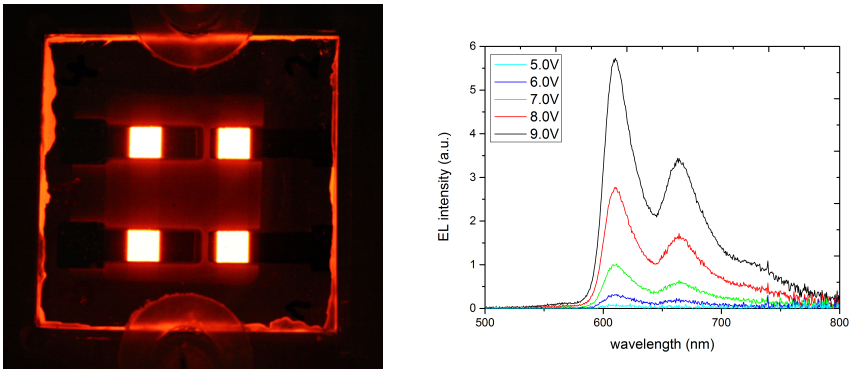

(a) 1 % DBP:Rubrene OLED (b) EL spectra

Figure 4.41: Image of the DBP:Rubrene OLED with a doping concentration of 1 % DBP powered at 6 V (a) and its voltage dependent EL spectra (b).

Fig. 4.42 shows an image of the 1 % DIP:Rubrene OLED powered at 6 V and the voltage-dependent EL spectra of this OLED. This orange, almost yellow OLED exhibit a peak intensity at 650 nm and a additional small shoulder at 550 nm. This shoulder is probably due to the emission of rubrene that could occur at this wavelength range.

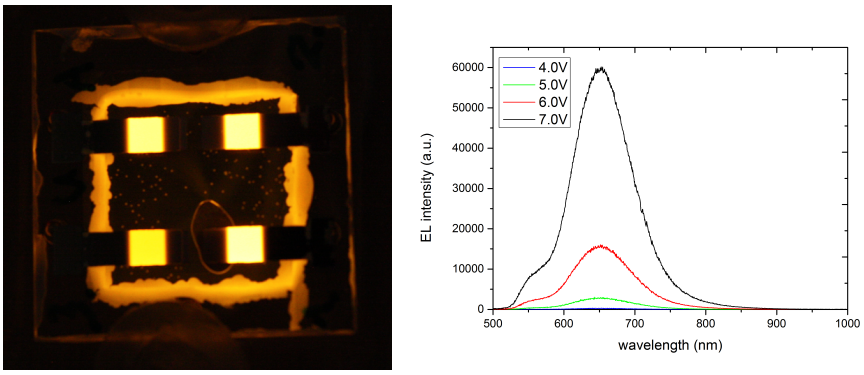

(a) 1 % DIP:Rubrene OLED (b) EL spectra

Figure 4.42: Image of the powered DIP:Rubrene OLED with a doping concentration of 1 % DIP powered at 6 V (a) and their voltage dependent EL spectra (b).

Fig. 4.43 shows the J-V-L of one pixel of both doped OLEDs. From the curve it can be extracted, that the short-circuit current density is rather small with 1E-3 mA/cm^2, the built-in voltage is 2.5 V for both OLEDs. The main difference of the two OLEDs is the value of the luminance that they reach at a driving voltage of 6 V. While for the doped

DBP OLED a value of 280 cd/m^2 was measured, the DIP doped OLED only reached a value of 50 cd/m^2.

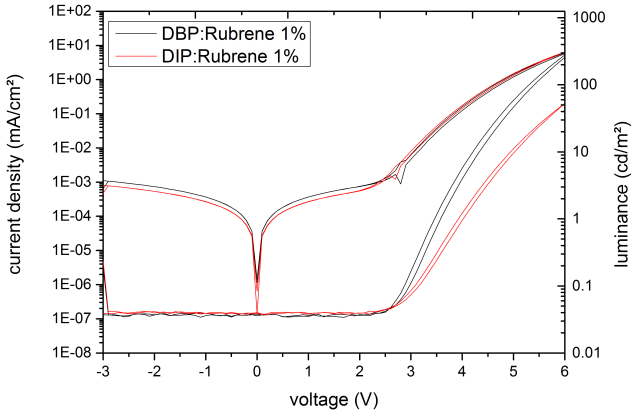

Figure 4.43: J-V-L-curve of one pixel of the two doped DBP (black lines) and DIP OLEDs (red lines).

This result is one hint, that the DBP if dissolved into rubrene as the matrix lead to higher efficiencies compared to the OLED with a EML comprising a doped DIP layer. In order to investigate this further EQE measurements were carried out. The results can be seen in Fig. 4.44.

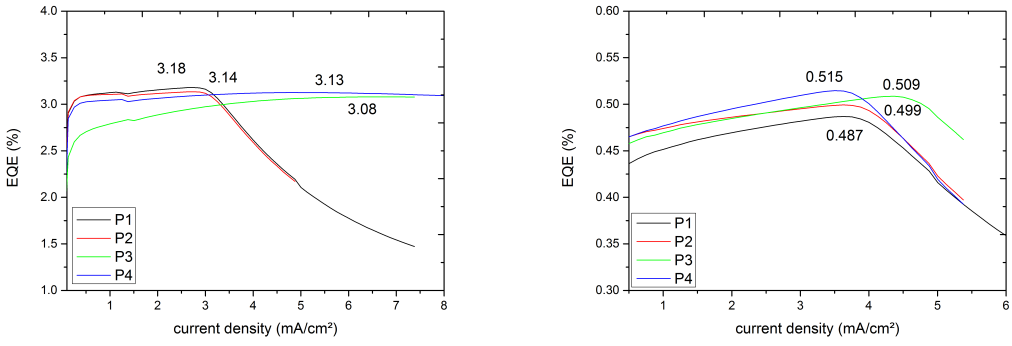

(a) 1 % DBP:Rubrene OLED

(b) 1 % DIP:Rubrene OLED

Figure 4.44: Results of the EQE measurement for all four pixels of the DBP:Rubrene 1 % OLED (a) and 1 % DIP:Rubrene OLED (b).

The doped DBP OLED reached EQE values of 3.2 % while a EQE of the doped DIP OLED was measured to be around 0.5 %. These values are quite high for fluorescent red emitters especially if you compare them with the EQE of a pure rubrene OLED. A value of only 0.2 % was reported by Okumoto *et al.* [27]. The horizontal trend of the EQE curves until a current density of at least 3.5 mA/cm^2 reveal that the charge-carrier balance is good in both OLED devices.
The measured value of the doped DBP OLED is smaller than the value reported by Okumoto *et al.* [27] with 4.7 %. A possible explanation for the difference could be the used ETL in this publication.
One factor that contribute to the difference in EQE values between the doped DBP and doped DIP OLEDs is the dipole orientation of the molecules within the doped EML. Because from Fig. 4.22 and Fig. 4.24 it could be extracted, that the orientation of the DBP molecules within the rubrene matrix is fully horizontal, while the DIP molecules show a rather isotropic orientation.

Now the un-polarised angle-resolved EL spectra of both doped OLEDs shall be examined and discussed. Fig. 4.45 illustrates the measured and simulated spectra of the doped DBP OLED without an attached prism. It was powered at 6 V during the measurement. Both spectra show the two pronounced peaks at 610 and 660 nm and their intensity decrease at higher angle values. The simulated spectrum is in good agreement with the measured one.

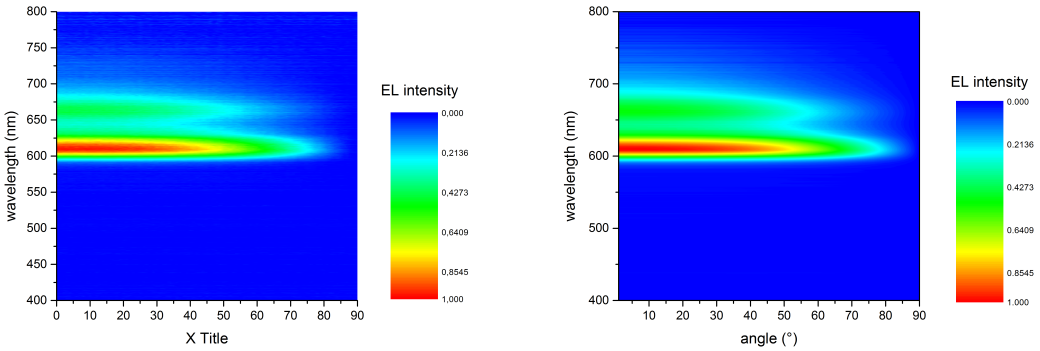

(a) measured spectrum (b) simulated spectrum

Figure 4.45: Measured and simulated angle-resolved un-polarised EL spectra of the doped DBP OLED without outcoupling prism.

In order to check if the doped DBP OLED acts like a Lambertian radiator a wavelength cut at 610 nm was performed (Fig. 4.46). From the emission profile it can be seen, that the doped DBP OLED shows aberrations compared to the emission profile of a Lambertian radiator.

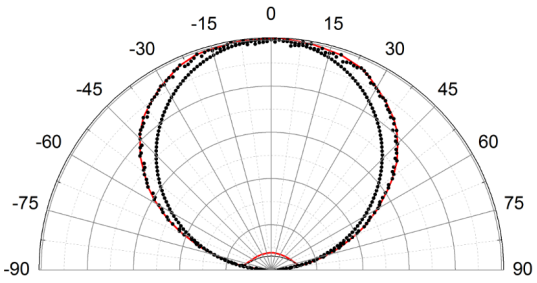

Figure 4.46: Cut of the EL spectrum of the DBP doped OLED (Fig. 4.45) at a wavelength of 610 nm (red line) compared to the emission profile of a Lambertian radiator (black line) between -90° and 90°.

Fig. 4.47 shows a cut at 610 nm of the measured (black line), simulated (blue line) un-polarised EL emission spectrum of the DIP OLED. Also the emission profile of a Lambertian radiator is included (red line). The emission profile reveal, that the DIP OLED can be characterised as a Lambertian radiator and the simulated profile is quite close to the measurement result. The aberrations between measurement and simulation are possibly due to the implemented layer thickness values in the simulation.

Now the result from the measurement and the simulation of the un-polarised angle-resolved EL emission spectra of the doped DIP OLED shall be discussed. The spectra were measured while the OLED was powered with 6 V. Both spectra without the use of a prism are displayed in Fig. 4.48. The spectra show a peak intensity at 640 nm that is decreasing towards larger angle values. If a cut at this maximum wavelength is performed Fig. 4.49 is obtained.

The emission profile reveal, that this doped DIP OLED acts as a Lambertian radiator or in other words the detected EL intensity does not depend on the viewing angle.

Fig. 4.50 shows a cut at 640 nm of the measured (black line), simulated (blue line) un-polarised EL emission spectrum of the doped DIP OLED. Also the emission profile of a Lambertian radiator is included (red line). The emission profile reveal, that the

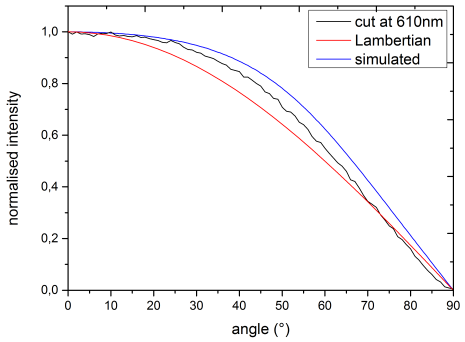

Figure 4.47: Cut of the EL spectrum of the doped DBP OLED (Fig. 4.45) (black line) and of the corresponding simulated spectrum (blue line) at a wavelength of 690 nm (red line) compared to the emission profile of a Lambertian radiator (red line) between 0° and 90°.

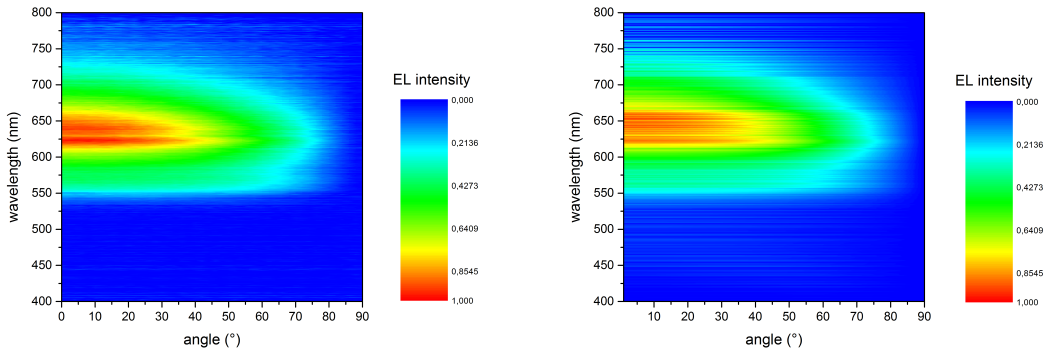

(a) measured spectrum

(b) simulated spectrum

Figure 4.48: Measured and simulated angle-resolved un-polarised EL spectra of the doped DIP OLED without outcoupling prism.

doped DIP OLED can be characterised as a Lambertian radiator and the simulated profile is quite close to the measurement result. The aberrations between measurement and simulation are possibly due to the implemented layer thickness values in the simulation.

At this point the fraction of power that is emitted at the different channels of the analysed doped OLEDs shall be presented and discussed. The result of the simulation of the analysed doped DBP and DIP OLED can be seen in Fig. 4.51.

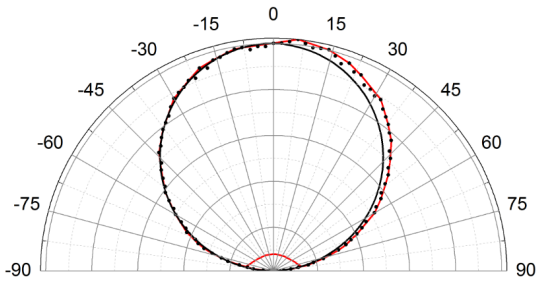

Figure 4.49: Cut of the EL spectrum of the DIP doped OLED (Fig. 4.48) at a wavelength of 640 nm (red line) compared to the emission profile of a Lambertian radiator (black line) between -90° and 90°.

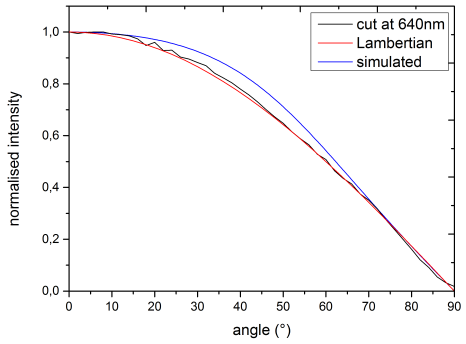

Figure 4.50: Cut of the EL spectrum of the doped DIP OLED (Fig. 4.48) (black line) and of the corresponding simulated spectrum (blue line) at a wavelength of 640 nm (red line) compared to the emission profile of a Lambertian radiator (red line) between 0° and 90°.

The doped DBP OLED emits 36 % of the created light directly to air, while 28 % is trapped in the substrate and 16 % within waveguide modes. 12 % of the power is lost due to the coupling to SPPs and 8 % is absorbed. The doped DIP OLED emits 25 % directly to air, 23 % to the substrate, 15 % is lost inside the waveguide modes and a value of 30 % is lost due to the near-field coupling to SPPs. The remaining 7 % is lost due to absoption. If a prism is used to outcouple the emission to the substrate 64 % of light can be extracted out of the doped DBP OLED, while 48 % can be extracted from the DIP OLED. These results can be connected to the results from the thin film and OLED characterisation, because the doped DBP EML with the pure horizontal dipole orientation lead to higher EQE values compared to the rather isotropic orientation of the DIP doped emission layer

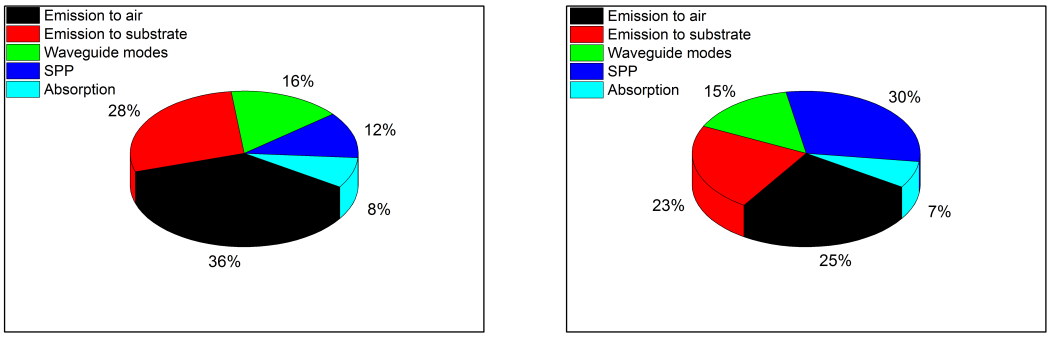

(a) doped DBP OLED

(b) doped DIP OLED

Figure 4.51: Ratio of the emitted power into the different optical channels of an OLED in the case of the doped DBP (a) and doped DIP OLED (b).

that couple stronger to surface plasmons.

At this point the results from the characterisation of the neat and doped films and the corresponding OLEDs shall be compared and discussed referring to table 4.1.

Table 4.1: Results of the characterisation of the neat and doped DBP and DIP films and the corresponding OLEDs in terms of orientation, amount of vertical p_z-dipoles for the films and luminance and EQE for the OLEDs.

Materials	**neat DBP**	**neat DIP**	**DBP:Rubrene**	**DIP:Rubrene**
Orientation	horizontal	vertical	horizontal	isotropic
Amount of p_z-dipoles (%)	5	52	0	23
Luminance (cd/cm²) at 6V	8.5	1.2	280	50
EQE (%)	0.20	0.04	3.2	0.52

From the results of the table it can be seen that the neat OLEDs show small values of the luminance and EQE compared to the doped OLEDs. The DBP molecules exhibit a horizontal orientation in the neat with 5 % vertical dipoles and in the doped films with no vertical dipoles. The DIP molecules show a vertical orientation in the neat with 52 % vertical dipoles and an isotropic orientation (23 % vertical dipoles) in the doped films. A possible explanation of the latter result could be, that the π-orbitals of the sigma-phase of

the standing molecules overlap, while this intermolecular interaction can not occur if they are dissolved into the rubrene matrix. A possible explanation for the huge increase of the efficiency from the neat to the doped OLEDs could be the very efficient Förster energy transfer from the rubrene matrix to the perylene based dyes.

5 Conclusion and outlook

The aim of this master thesis was to investigate a possible link between the dipole orientation of perylene based films and the efficiency of corresponding OLEDs. Also the effect of the substrate temperature on the molecular orientation and OLED efficiency was investigated.

The results of the neat thin film characterisation reveal, that DBP absorbs more light within the visible region, that it is fully amorphous and that it exhibits a rather smooth surface. The DIP films show a comparable weak absorption behavior, are polycrystalline and exhibit a rather rough surface. The absorption, crystallographic phase and topographic results did not change if both materials were deposited onto α-NPD as the hole transport layer. Angle-dependent PL measurement of the thin perylene films reveal, that the DBP molecules show a horizontal orientation with only 5 % vertical dipoles while a large fraction of the DIP molecules (52 %) appear to stand upright. This result can also explain the high coupling strength of the DIP molecules to surface plasmons compared to the coupling of DBP molecules.

OLEDs comprising neat films of DBP and DIP were shown to exhibit small EQE values of 0.2 and 0.04 %. One reason for the differences in efficiency could be explained by the dipole orientation, which lead to a higher outcoupling factor of 27 % of the DBP OLED compared to 16 % of the DIP OLED. Angle-dependent EL measurements of both OLEDs show, that there is a good agreement between performed simulations and the measurement results. The DIP OLED was found to represent a Lambertian emission profile while a huge aberration was detected for the DBP OLED. This result could also be explained by the molecular orientation.

The results if the substrate was heated to a temperature of 87°C during the deposition of DBP and DIP lead to a loss in orientation of the molecules. The amount of vertical dipoles was determined to increase in the case of the heated DBP layer to a value of 9 % vertical dipoles and to decrease in the case of the DIP layer to a value of 44 % vertical dipoles. OLEDs where only the hole transport layer was heated prior to the deposition showed

smaller EQE values in the case of the DBP EML while this processing step had no big influence on the efficiency of DIP OLEDs. If the substrate was heated duringt the growth of the DBP and DIP EML it lead to an increase of the EQE to a value of around 0.3 % for the DBP and to 0.06 % for the DIP OLED. A possible explanation for the increase in the case of the heated DBP OLED is the improved charge-carrier balance. The increase for the heated DIP OLED can be attributed to the improved emitter orientation.
In order to analyse the molecular orientation and OLED efficiency a fraction of 1 % of DBP and DIP was doped into rubrene as the host material. Thin doped films were investigated by angle-dependent PL measurements to gain information about the molecular orientation. The orientation of the DBP molecules within the doped film was measured to be fully horizontal, while the DIP molecules exhibit a vertical dipole ratio of 23 % that is close to an isotropic orientation.
The detected orientation is one reason for the huge increase in efficiency with EQE values of 3 % for the doped DBP OLED and 0.5 % for the doped DIP OLED.
The angle-resolved EL measurements of both doped OLEDs reveal, that they show a Lambertian emission profile.
In general it can be said that the emitter orientation has a huge effect on the OLED efficiency in perylene based OLEDs and lead to a remarkable increase of light-outcoupling of 70 % in the case of the neat EML and 44 % in the case of the doped EML. The EQE values of OLEDs with neat EML could be increased by a factor of 5 and by OLEDs with doped EML by a factor of 6 if the values of table 4.1 are compared.

In order to further understand the effect of elevated substrate temperature on the emitter orientation and efficiency of perylene based OLEDs thin films produced at different substrate temperatures should be analysed in terms of emitter orientation and morphology and the EQE values of corresponding OLEDs be measured.
The reason for the huge increase of the EQE values of the doped EML OLEDs compared to the neat EML OLEDs has to be investigated. A possible explanation could be the very efficient energy transfer from the rubrene matrix to the perylene based dye.
Apart from this also the effective radiative quantum efficiency of the neat and the doped OLEDs should be determined to really make a quantitative statement of how much the emitter orientation contribute to this increase in efficiency from the DIP with a vertical or isotropic orientation to the DBP with a horizontal emitter orientation.

Bibliography

[1] C. Mayr. Einfluss der molekularen Orientierung in organischen Leuchtdioden. Master's thesis, University of Augsburg, 2011.

[2] N. Labanca P. Bertoldi, B. Hirl. Energy efficiency status report 2012. Technical report, European Union Report EUR 25405 EN, 2012.

[3] C. W. Tang and S. A. VanSlyke. Organic electroluminescent diodes. *Applied Physics Letters*, 51(12):913–915, 1987.

[4] M. Flämmich, J. Frischeisen, D. S. Setz, D. Michaelis, B. C. Krummacher, T. D. Schmidt, W. Brütting, and N. Danz. Oriented phosphorescent emitters boost oled efficiency. *Organic Electronics*, 12(10):1663 – 1668, 2011.

[5] J. Frischeisen, D. Yokoyama, A. Endo, C. Adachi, and W. Brütting. Increased light outcoupling efficiency in dye-doped small molecule organic light-emitting diodes with horizontally oriented emitters. *Organic Electronics*, 12(5):809 – 817, 2011.

[6] W. Brütting. *Physics of Organic Semiconductors*. Viley-VCH, 2005.

[7] H.C. Wolf and M. Schwörer. *Organic Molecular Solids*. Viley-VCH, 2007.

[8] W. Brütting, S. Berleb, and A. G. Mueckl. Device physics of organic light-emitting diodes based on molecular materials. *Organic Electronics*, 2(1):1 – 36, 2001.

[9] T. Tsutsui, E. Aminaka, C. P. Lin, and D. U. Kim. Extended molecular design concept of molecular materials for electroluminescence: sublimed–dye films, molecularly doped polymers and polymers with chromophores. *Philosophical Transactions of the Royal Society of London. Series A:Mathematical, Physical and Engineering Sciences*, 355(1725):801–814, 1997.

[10] S. Nowy, B. C. Krummacher, J. Frischeisen, N. A. Reinke, and W. Brütting. Light extraction and optical loss mechanisms in organic light-emitting diodes: Influence of the emitter quantum efficiency. *Journal of Applied Physics*, 104(12):123109–123109–9, 2008.

[11] J. Frischeisen. *Light extraction in organic light-emitting diodes*. PhD thesis, University of Augsburg, 2011.

[12] R. P.Van Duyne. Molecular plasmonics. *Science*, 305:985–986, 2004.

[13] J. R. Sambles, G. W. Bradbery, and Fuzi Yang. Optical excitation of surface plasmons: An introduction. *Contemporary Physics*, 32(3):173–183, 1991.

[14] R. Brune. *Grenzen und Möglichkeiten des Förster Resonanz-Energietransfer*. PhD thesis, Universität Bielefeld, 2009.

[15] C.C. Wu, C. I. Wu, J.C. Sturm, and A. Kahn. Surface modification of indium tin oxide by plasma treatment: An effective method to improve the efficiency, brightness, and reliability of organic light emitting devices. *Applied Physics Letters*, 70(11):1348–1350, 1997.

[16] X. Crispin, F. L. E. Jakobsson, A. Crispin, P. C. M. Grim, P. Andersson, A. Volodin, C. van Haesendonck, M. Van der Auweraer, W. R. Salaneck, and M. Berggren. The origin of the high conductivity of poly(3,4-ethylenedioxythiophene)-poly(styrenesulfonate) (pedot-pss) plastic electrodes. *Chemistry of Materials*, 18(18):4354–4360, 2006.

[17] J. Wagner, M. Gruber, A. Hinderhofer, A. Wilke, B. Bröker, J. Frisch, P. Amsalem, A. Vollmer, A. Opitz, N. Koch, F. Schreiber, and W. Brütting. High fill factor and open circuit voltage in organic photovoltaic cells with diindenoperylene as donor material. *Advanced Functional Materials*, 20(24):4295–4303, 2010.

[18] X. Xiao, J. D. Zimmerman, B. E. Lassiter, K. J. Bergemann, and S. R. Forrest. A hybrid planar-mixed tetraphenyldibenzoperiflanthene/c70 photovoltaic cell. *Applied Physics Letters*, 102(7):073302–073302–4, 2013.

[19] D. Käfer and G. Witte. Growth of crystalline rubrene films with enhanced stability. *Phys. Chem. Chem. Phys.*, 7:2850–2853, 2005.

[20] T. Takahashi, T. Takenobu, J. Takeya, and Y. Iwasa. Ambipolar organic field-effect transistors based on rubrene single crystals. *Applied Physics Letters*, 88(3):033505–033505–3, 2006.

[21] S. Naka, H. Okada, H. Onnagawa, and T. Tsutsui. High electron mobility in bathophenanthroline. *Applied Physics Letters*, 76(2):197–199, 2000.

[22] V. E Choong, M. G. Mason, C.W. Tang, and Yongli Gao. Investigation of the interface formation between calcium and tris-(8-hydroxy quinoline) aluminum. *Applied Physics Letters*, 72(21):2689–2691, 1998.

[23] G.E. Jabbour, Y. Kawabe, S.E. Shaheen, J.-F. Wang, M.M. Morrell, B. Kippelen, and N. Peyghambarian. Highly efficient and bright organic electroluminescent devices with an aluminum cathode. *Applied Physics Letters*, 71(13):1762–1764, 1997.

[24] A. R. Brown, D. D C Bradley, J.H. Burroughes, R.H. Friend, N.C. Greenham, P.L. Burn, A.B. Holmes, and A. Kraft. Poly(pphenylenevinylene) light-emitting diodes: Enhanced electroluminescent efficiency through charge carrier confinement. *Applied Physics Letters*, 61(23):2793–2795, 1992.

[25] H. Y. Cho, L. S. Park, Y. S. Han, Y. Kwon, and J.-Y. Ham. High-t g n-triarylamine derivatives as a hole injecting layer in organic light-emitting diodes. *Molecular Crystals and Liquid Crystals*, 499(1):1/[323]–10/[332], 2009.

[26] M. Horlet, M. Kraus, W. Brütting, and A. Opitz. Diindenoperylene as ambipolar semiconductor: Influence of electrode materials and mobility asymmetry in organic field-effect transistors. *Applied Physics Letters*, 98(23):233304–233304–3, 2011.

[27] K. Okumoto, H. Kanno, Y. Hamada, H. Takahashi, and K. Shibata. High efficiency red organic light-emitting devices using tetraphenyldibenzoperiflanthene-doped rubrene as an emitting layer. *Applied Physics Letters*, 89(1):013502–013502–3, 2006.

[28] D. Y. Kondakov. Voltammetric study of bphen electron-transport layer in contact with lif/al cathode in organic light-emitting diodes. *Journal of Applied Physics*,

99(2):024901, 2006.

[29] Jr. William D. Callister. *Materials Science and Engineering*. John Wiley & Sons, Inc., 2007.

[30] E. Meyer. Atomic force microscopy. *Progress in Surface Science*, 41(1):3 – 49, 1992.

[31] J. Frischeisen, D. Yokoyama, C. Adachi, and W. Brütting. Determination of molecular dipole orientation in doped fluorescent organic thin films by photoluminescence measurements. *Applied Physics Letters*, 96(7), FEB 15 2010.

[32] T. Körner. *Integration magnetooptisch aktiver Granate auf Nicht-Granat-Substraten*. PhD thesis, Universtiät Augsburg, 2008.

[33] B. Lebsanft. Bestimmung der Quanteneffizienz organischer Farbstoffe über ihre Lumineszenzlebensdauer. Master's thesis, University of Augsburg, 2010.

[34] A. Sommerfeld. Über die Ausbreitung von Wellen in der drahtlosen Telegraphie. *Annalen der Physik*, 28:665 – 736, 1909.

[35] Z. Wang, D. Yokoyama, X.-F. Wang, Z. Hong, Y. Yang, and J. Kido. Highly efficient organic p-i-n photovoltaic cells based on tetraphenyldibenzoperiflanthene and fullerene c70. *Energy Environ. Sci.*, 6:249–255, 2013.

[36] B. E. Koene, D. E. Loy, and M. E. Thompson. Asymmetric triaryldiamines as thermally stable hole transporting layers for organic light-emitting devices. *Chemistry of Materials*, 10(8):2235–2250, 1998.

[37] M. Carrard, S. Goncalves-Conto, L. Si-Ahmed, D. Adès, and A. Siove. Improved stability of interfaces in organic light emitting diodes with high tg materials and self-assembled monolayers. *Thin Solid Films*, 352:189 – 194, 1999.

[38] D. Yokoyama, Z. Qiang Wang, Y.-J. Pu, K. Kobayashi, J. Kido, and Z. Hong. High-efficiency simple planar heterojunction organic thin-film photovoltaics with horizontally oriented amorphous donors. *Solar Energy Materials and Solar Cells*, 98(0):472 – 475, 2012.

[39] M. Shakutsui, H. Matsuura, and K. Fujita. Improved efficiency of polymer light-emitting diodes by inserting a hole transport layer formed without thermal treatment above glass transition temperature. *Organic Electronics*, 10(5):834 – 842, 2009.

[40] M. Uchida, C. Adachi, and Y. Koyama, T.and Taniguchi. Charge carrier trapping effect by luminescent dopant molecules in single-layer organic light emitting diodes. *Journal of Applied Physics*, 86(3):1680–1687, 1999.